Journal of Alloys and Compounds 1080 (2026) 190804

Contents lists available at ScienceDirect

Journal of Alloys and Compounds

journal homepage: www.elsevier.com/locate/jalcom

Exploration of high-entropy alloys and metallic glasses in the Hf-Nb-Ta-Ti-V-Zr compositional library using a sputtered combinatorial layer

Ao Wang [a], László Pethö [b], Zoltán Hegedűs [c], Maria Wątroba [b], Jorge de Oliveira [b], Zsolt Czigány [d], Johann Michler [b], Jenő Gubicza [a,*]

[a] Department of Materials Physics, ELTE Eötvös Loránd University, P.O. Box 32, Budapest, H-1518, Hungary
[b] EMPA Swiss Federal Laboratories for Materials Science and Technology, Laboratory for Mechanics of Materials and Nanostructures, Feuerwerkerstrasse 39, Thun, CH-3602, Switzerland
[c] Deutsches Elektronen-Synchrotron DESY, Hamburg, 22607, Germany
[d] Institute of Technical Physics and Materials Science, HUN-REN Centre for Energy Research, Konkoly Thege M. út 29-33, Budapest, H-1121, Hungary

ARTICLE INFO

Keywords:
High-entropy alloy
Hf-Nb-Ta-Ti-V-Zr compositional library
Combinatorial layer
Magnetron sputtering
Nanoindentation

ABSTRACT

A Hf-Nb-Ta-Ti-V-Zr combinatorial layer was studied in order to explore different high-entropy alloys and metallic glasses in this refractory compositional library. The film with a thickness of about 2 μm was deposited on a Si single crystal wafer by magnetron sputtering. The minimum and maximum concentrations of the different elements were in the ranges of 3–7% and 26–52%, respectively. The phase composition and the microstructure as a function of the chemical composition were mapped by synchrotron X-ray diffraction and transmission electron microscopy. The mechanical performance was examined by nanoindentation for the different compositions. It was found that the majority of the studied compositions (about 80%) exhibited amorphous structures due to the large atomic size mismatch. Single phase body-centered cubic (BCC) structure developed only in the vicinity of the Ti/Ta/Nb targets while BCC matrix with ω secondary phase formed close to the Hf target. The crystalline columns in the BCC region have dome-shaped caps and exhibited chemical heterogeneities due to the shadowing effect. The highest hardness (5.9 ± 0.3 GPa) was observed in the amorphous region close to the V source due to the low atomic radius and high VEC of this element.

1. Introduction

High-entropy alloys (HEAs) are a promising new generation of alloy systems that break away from traditional alloy design strategies [1]. It increases the number of major elements to five or more, with each element having a concentration between 5 and 35 at. percent, typically present in equimolar ratios [2]. By definition, HEA is considered if its configurational entropy is higher than $1.5 \times R$ (where R is the universal gas constant) [3]. The high configurational entropy can effectively suppress the formation of complex intermetallic compounds under conditions of severe atomic size mismatch and lattice distortion, promoting the development of simple phases of HEAs [4]. Examples include CoCrFeNi [5], CoCrMnNi [6], AlTiVNb [7], and PtPdRhRuIr series [8]. Special HEAs based on refractory metal elements (refractory high-entropy alloys, RHEAs) can maintain mechanical strength at high temperatures, attracting significant research attention. The standard definition of refractory metals includes five elements with melting points greater than 2400 °C: Nb, Mo, Ta, W and Re, while a broader definition includes nine additional elements with melting points greater than 1650 °C (Ti, V, Cr, Zr, Ru, Rh, Hf, Os and Ir) [9].

In recent years, the Hf-Nb-Ta-Ti-Zr RHEA system has attracted much attention due to its unique combination of high-temperature strength and ductility [10–12]. Senkov *et al.* [13,14] prepared HfNbTaTiZr RHEA, which exhibited compressive strain > 50% at room temperature. Krnel *et al.* [9] improved the mechanical properties of HfNbTaTiZr RHEA by introducing Sc, but the sample separated into body-centered cubic (BCC) and hexagonal close-packed (HCP) phases. Huang *et al.* [15] demonstrated that the presence of Nb is beneficial for maintaining a single BCC structure in the alloy. Yurchenko *et al.* [16] reported that the addition of Ta improved the fracture toughness and oxidation

* Corresponding author.
E-mail address: jeno.gubicza@ttk.elte.hu (J. Gubicza).

https://doi.org/10.1016/j.jallcom.2026.190804
Received 3 July 2026; Received in revised form 17 August 2026; Accepted 28 August 2026
Available online 29 August 2026

resistance, while the addition of V reduced the oxidation resistance. Liang *et al.* [17] demonstrated through molecular dynamics guided design and additive manufacturing that reducing Ta decreases tensile strength, while reducing Hf increases it. However, simultaneously reducing both Hf and Ta decreases elastic modulus and strength, highlighting the system's high sensitivity to composition. Wang *et al.* [18] pointed out that excessive V addition leads to instability in the BCC structure of $NbTiV_xZr$ samples, but with increasing V content, the hardness increases due to solid solution strengthening. In addition, Chen *et al.* [19] prepared a series of NbMoCrTiAl RHEAs and reported a near-linear relationship between microhardness and atomic size mismatch. Due to the smaller atomic radius of V compared with other constitutional elements, with the introduction of V element, the hardness is expected to be higher.

In summary, previous studies indicate that alloys in the Hf-Ta-Ti-Nb-V-Zr compositional library possess unique characteristics within RHEAs, and their phase stability and mechanical properties are strongly influenced by elemental composition. Tomáš *et al.* [20] successfully prepared equimolar HfNbTaTiVZr RHEAs via vacuum arc melting, demonstrating that V-containing hexa-element RHEAs represent a feasible high-entropy solid solution system. However, former researches mostly focused on property changes resulting from altering only a few elements. For instance, Chen *et al.* [21] prepared $HfZrTi(TaNbV)_x$ HEAs and found that with increasing Ta, Nb, and V content, the grain size gradually decreased. This grain refinement resulted in better tensile properties, and the accompanying lattice distortion further enhanced yield strength. However, this approach fails to provide a complete compositional library for the studied system. A more detailed characterization of compositional libraries can be performed by the processing and study of combinatorial multi-principal element alloy (MPEA) films. By synthesizing multicomponent alloys with well-defined concentration gradients, the effects of constituent elements on the crystal structure and mechanical properties can be efficiently studied. Former studies have proved the effectivity of combinatorial sample in the exploration of different compositional libraries, e.g., Co-Cr-Cu-Fe-Ni-Zn [22] and Co-Cr-Fe-Mo-Ni-W [23]. More details about the combinatorial design of novel HEAs can be found in Ref. [24]. However, the exploration of the phase composition and the mechanical properties in the whole Hf-Ta-Ti-Nb-V-Zr compositional library has not been performed yet.

This work aims to investigate a six-component Hf-Ta-Ti-Nb-V-Zr combinatorial thin film system and map the influence of the chemical composition on the phase content, microstructure and mechanical performance, in order to extend the investigation of Hf-Ta-Ti-Nb-V-Zr series with more different compositions. The concentration of each element varies between 3–7% and 26–52%. Such a large range of element concentrations within a single sample can not be achieved in bulk combinatorial samples processed by either traditional methods (e.g., heat treatment of diffusion couples) or novel techniques (e.g., additive manufacturing). Therefore, in this study co-deposition of the six constituent elements using magnetron sputtering was applied for obtaining a wide range of chemical compositions. The coating was deposited onto the surface of a Si wafer with a diameter of 10 cm. The large sample dimension facilitates the study of the compositional space with a good resolution by different experimental techniques. X-ray fluorescence (XRF) spectroscopy and synchrotron X-ray radiation are used to map the chemical and phase compositions, respectively. The microstructure for some selected compositions is characterized by transmission electron microscopy (TEM). The mechanical performance is mapped by nano-indentation, and the correlation between the structural parameters and the mechanical behavior is discussed in detail.

2. Methods

2.1. Processing of the combinatorial sample by magnetron sputtering

The preparation of the six-component combinatorial Hf-Ta-Ti-Nb-V-Zr thin film was performed using a Hex-L hexagonal chamber (Korvus Technology Ltd., High Wycombe, UK) configured in a sputter-up arrangement. The chamber is equipped with six 2-inch magnetrons, positioned on each side panel at 60° intervals. Each magnetron utilized a target disk of 50 mm in diameter and 3 mm in thickness with a purity exceeding 99.95%, sourced from HMW-Hauner GmbH, Röttenbach, Germany. A 10 cm diameter silicon single-crystal substrate with a $< 100 >$ orientation was employed, maintained in a stationary horizontal position during deposition to achieve a combinatorial sample. The Si single crystal substrate was coated with a 100 nm thick amorphous SiN_x layer. The targets were placed below the substrate plane. The spacing between the centers of the targets and the plane of the substrate disk was 50 mm. The distance between center the substrate disk and the centers of the targets in horizontal direction was 110 mm. The targets are tilted at 20° to the horizontal plane of the substrate. Before the deposition, the chamber achieved a base pressure of 8×10^{-7} mbar. The deposition process is conducted with an argon flow rate of 40 sccm, uniformly distributed among the magnetrons, at a process pressure of 10^{-2} mbar for a duration of 1 h. Plasma parameters for each target material are detailed in Table S1 in the Supplementary material. The magnetrons are powered by TDK Lambda DC sources operating in current control mode. Individual deposition rate characterizations are performed for each element to establish the current setpoint values for the magnetrons. Plasma parameters are optimized to achieve an equimolar composition at the substrate's center, corresponding to the confocal point of the magnetron arrangement.

2.2. Mapping the chemical composition

The fully automated XRF mapping of the substrate was performed using the custom-built SwissMapper instrument. A total of 617 regularly spaced points at 3.5 mm pitch were recorded. XRF data were collected using an integrated, inverted Fischerscope XAN 250 energy-dispersive X-ray fluorescence spectrometer equipped with a micro-focus Tungsten tube and a Silicon Drift Detector. Measurements were collected with an exposure time of 30 s per point. The instrument operated at a tube voltage of 50 kV, using a 0.3 mm collimator and a Ni primary filter. Quantification of elemental concentrations was performed using the instrument's fundamental parameter method software (WinFTM). The quantification model assumed a two-layer structure: a top layer comprising the film and a substrate layer of Si to represent the wafer. For thickness evaluations, the standard densities of the constituent pure metals were used.

2.3. Determination of the phase and microstructure maps

The microstructure was investigated using synchrotron X-ray diffraction (XRD) at the Deutsches Elektronen-Synchrotron (DESY) in Hamburg, Germany. The measurements were performed with a beam energy of 52 keV, corresponding to the wavelength of $\lambda = 0.023843$ nm. The measurement points were arranged in a rectangular grid with a 2 mm spacing along both the horizontal (X-axis) and vertical (Z-axis) directions. The origin of this X-Z Cartesian coordinate system was attached to the center of the disk. Due to the fixation of the disk during sputtering and the subsequent measurements, not the whole circular area was studied. Therefore, the ranges of coordinates related to the disk points were different in directions X and Z. Namely, the XRD patterns were collected over the horizontal range of X = -50–50 mm and the vertical range of Z = -45–45 mm with spacing 2 mm, yielding a total of 9191 measurement points. The X-ray beam spot size on the sample surface measured 0.75 mm along both X- and Z-directions. The phase map of the coating is determined based on these XRD patterns. Detailed analysis of the microstructure was performed by TEM including high resolution TEM (HR-TEM) and selected area electron diffraction (SAED) using a Cs corrected Thermo Fisher Themis TEM (Thermo Fisher Scientific, Waltham, MA, USA). The analysis was performed at 200 kV

accelerating voltage with point resolution of 0.08 nm. High angle annular dark field (HAADF) images and energy-dispersive X-ray spectroscopy (EDS) elemental maps on the film cross section were recorded in scanning transmission electron microscopy (STEM) mode. The microscope is equipped with four Thermo Fisher EDS detectors in Super-X geometry. The preparation of the TEM specimens was done by focused ion beam (FIB) using Thermo Fisher Scientific Scios 2 Dual Beam equipment. The final steps in FIB preparation were made at 2 kV.

2.4. Nanoindentation

Mechanical characterization was performed via nanoindentation employing an ex-situ scanning nanoindenter (Alemnis AG) with a Berkovich diamond tip (Synton MDP) at locations spaced 3.54 mm apart across the film surface to evaluate spatial variation in hardness and elastic modulus. Six indents were performed at each location to provide statistical reliability of the measurements. The maximum displacement was limited to 160 nm, corresponding to less than 10% of the film thickness, thereby ensuring negligible substrate contribution to the measured properties. The load corresponding to this penetration depth limit varied between 6 and 8 mN, depending on the mechanical properties of the tested composition in the combinatorial disk. Load-displacement curves were evaluated using AMMDA software (Alemnis AG, Thun, Switzerland) supplemented by custom Python scripts for data processing. Elastic modulus and hardness were extracted from the load-displacement data according to the Oliver-Pharr analysis framework [25], with a Poisson's ratio of $\nu = 0.4$ adopted for the calculations [26].

3. Results

3.1. Compositional and phase mapping of the combinatorial sample

The concentration distribution of constituent elements within the coating is investigated using XRF spectroscopy. The obtained elemental maps are shown in Fig. 1. The concentrations of Hf, Ta, Ti, Nb, V, and Zr vary in the ranges of 7–47%, 3–41%, 3–45%, 3–26%, 7–52%, and 5–44%, respectively (all chemical compositions in this study are given in at%). Additionally, the map of layer thickness values is also obtained by XRF spectroscopy, as shown in Fig. S1 in the Supplementary material. The thickness of the coating ranges from 1683 ± 30 nm to 2695 ± 40 nm, with the maximum thickness observed in the proximity to the Hf target. The overall coating is thicker at the periphery than in the center due to the higher deposition rate closer to the targets.

The phase composition was determined from the XRD patterns. It is noted that the penetration depth of XRF technique is greater than the studied layer thickness, thus the concentration values presented in Fig. 1 characterize the whole thickness of the film. The same is valid for XRD; therefore, the study of the correlation between the chemical composition determined by XRF and the structural parameters (e.g., lattice constants) obtained by XRD has a sense. Depending on the chemical composition, BCC, omega (HCP structure, space group P6/mmm, ω) and amorphous (AP) phases were identified in the different points (see Fig. 2**a**). Fig. 2**b-d** shows typical XRD patterns for points with BCC, BCC + ω and AP structures. The insets in Fig. 2**b-d** reveal that in the two-dimensional diffraction patterns the Debye-Scherrer rings of the layer strongly overlap with the diffraction spots and the Kikuchi bands of the Si single crystal substrate. In order to minimize the substrate effect on the results obtained from the XRD patterns, the left-hand sector region concentric with the diffraction rings was used for the evaluation (indicated with bright contrast in the insets of Fig. 2**b-d**). In this sector, there are no high intensity diffraction spots of the Si substrate. The intensity in this sector was integrated along the Debye-Scherrer rings, and thus a diffraction pattern (intensity versus scattering angle, 2θ) was obtained for each studied point of the layer. The broad peaks related to the Kikuchi bands of the Si substrate were considered as parts of the background when evaluating the XRD patterns. It is noted that for amorphous structures having similar broad diffraction peaks, the diffraction pattern was also confirmed by TEM as shown later in this study. The phase map in Fig. 2**a** reveals a single-phase BCC region close to the Ta/Ti/Nb targets as well as a BCC + ω region in the vicinity of the Hf target. Otherwise, most of the layer is amorphous (AP area), and there are intermediate two/three-phase regions. The majority of the studied compositions (about 80%) exhibited amorphous structures. This ratio is estimated from the area fraction of the phase map shown in Fig. 2**a**. The peaks 100, 101, 002, 110 and 200 of the ω phase are marked in order in Fig. 2**d**. It is noted that there is an uncertainty in the position of the phase boundaries between the crystalline and the amorphous regions since it is hard to determine when the broad peaks of the AP phase under the crystalline peaks perfectly disappear.

The lattice constant of the BCC phase in the BCC single phase region close to the Ti target and in the BCC+ω phase area in the vicinity of the Hf target was determined from the XRD peak positions. The lattice constant values are plotted in the maps shown in Fig. 3. It is worth noting that the lattice parameter values were determined in those points only where XRF spectroscopy measurement was also performed. The lattice constants for other points in the map were obtained by interpolation and extrapolation using the Renka-Cline interpolation method in Origin software (Supplier: OriginLab Co., Northampton, USA). Thus,

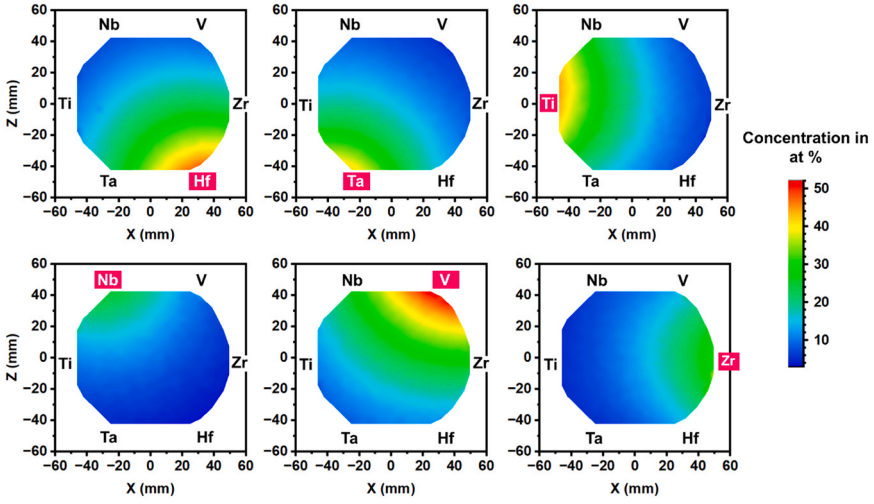

Fig. 1. Concentration distribution maps of the constituent elements determined by XRF for the combinatorial Hf-Ta-Ti-Nb-V-Zr coating. The chemical symbols around the maps mark the approximate positions of the targets in magnetron sputtering.

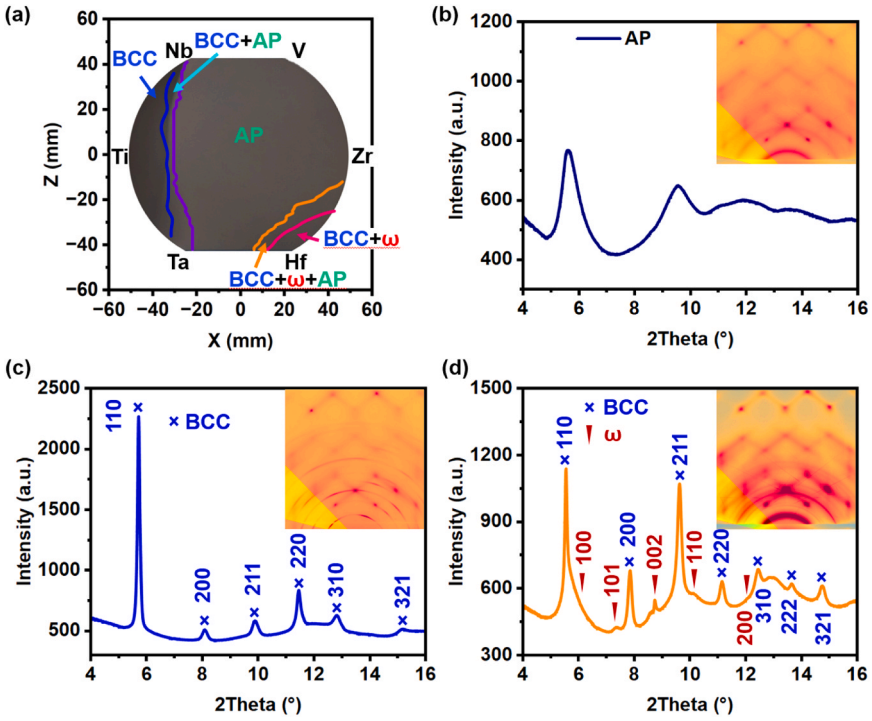

Fig. 2. (a) Schematic representation of the phase map for the combinatorial Hf-Ta-Ti-Nb-V-Zr coating. (b-d) Typical XRD patterns are shown for points with AP, BCC and BCC + ω structures. The coordinates of the points where these patterns were obtained are the following: X = 21.24, Z = 21.24 (AP); X = -38.94, Z = 10.62 (BCC); X = 28.32, Z = -35.4 (BCC+ω). The insets in b-d show the two-dimensional diffraction patterns containing the Debye-Scherrer rings of the layer as well as the diffraction spots and the Kikuchi bands of the Si single crystal substrate. In order to minimize the substrate effect on the results obtained from the XRD patterns, the left-hand sector region concentric with the diffraction rings was used for the evaluation (indicated with bright contrast in the insets of figures b-d.

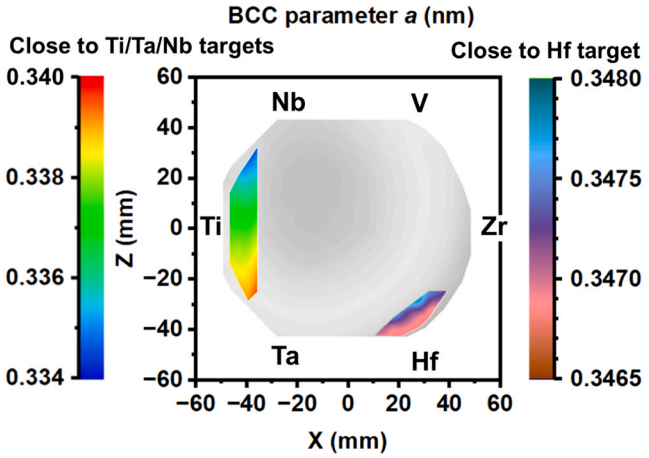

Fig. 3. Map of the lattice parameter of the BCC phase in two regions of the coating. The relative errors of the lattice constant values are about ± 0.05%. The colored areas are related to the fully BCC regions only while the multiphase or amorphous areas are shown with light gray where the lattice constant was not determined.

lattice constant values are also plotted in the areas out of the experimentally studied points at the perimeter of the disk. The lattice constant a in the single phase BCC region close to the Ti target varied between 0.3345 ± 0.0005 nm and 0.3396 ± 0.0002 nm while that in the BCC + ω phase region was between 0.3468 ± 0.0003 nm and 0.3478 ± 0.0002 nm. In the single phase BCC area, the lattice constant a reached its largest value near the Ta target and gradually decreased in the direction of the Nb target. This effect was observed because the points near the Ta target are also close to the Hf target, and the atomic radius of Hf (159 pm) is much larger than that of Ta (142 pm), Nb (142 pm) or Ti (147 pm). For the BCC + ω region, the lattice constant a reaches the maximum value near the Hf and Zr targets and decreases towards the center of the coating, though this variation is very low. This is because the atomic radii of Hf (159 pm) and Zr (160 pm) are almost identical, while the others are much smaller.

3.2. *Influence of chemical composition on mechanical behavior as obtained by nanoindentation*

The maps of hardness and elastic modulus determined by nanoindentation are shown in Fig. 4. There are 574 points where the indentation test was performed. In other points of the map, the hardness and elastic modulus values were obtained by interpolation and extrapolation using the Renka-Cline interpolation method in Origin software. The highest hardness (5.9 ± 0.3 GPa) and elastic modulus (111 ± 7 GPa) were observed in the AP region near the V and Nb targets, respectively. The chemical compositions at these two locations are 11.4% Hf – 7.9% Ta – 13.4% Ti – 13.8% Nb – 40.3% V – 13.2% Zr (highest hardness) and 13.0% Hf – 11.5% Ta – 15.3% Nb – 20.5% Ti – 29.1% V – 10.6% Zr (highest elastic modulus). The uncertainty of the concentration values is 0.1%. The lowest hardness (2.8 ± 0.2 GPa) and the lowest elastic modulus (76 ± 6 GPa) were detected in the BCC + AP area with the composition of 10.1% Hf – 12.5% Ta – 31.9% Ti – 17.6% Nb – 21.1% V – 6.8% Zr. Similar low elastic modulus was observed in the amorphous area with the composition of 14.1% Hf – 6.5% Ta – 6.9% Ti – 6.7% Nb – 41.9% V – 23.8% Zr. In summary, the single-phase BCC and BCC + AP regions exhibited significantly lower hardness values (between 2.8 and 3.9 GPa) compared to the other areas in the disk. The hardness value of the BCC + ω phase region was higher at around 5 GPa. Furthermore, the elastic modulus decreases near the Zr/Hf targets, likely due to their lower intrinsic elastic moduli of these constituents compared to other elements. It is noted that in the determination of the elastic modulus from nanoindentation the value of the Poisson's ratio is

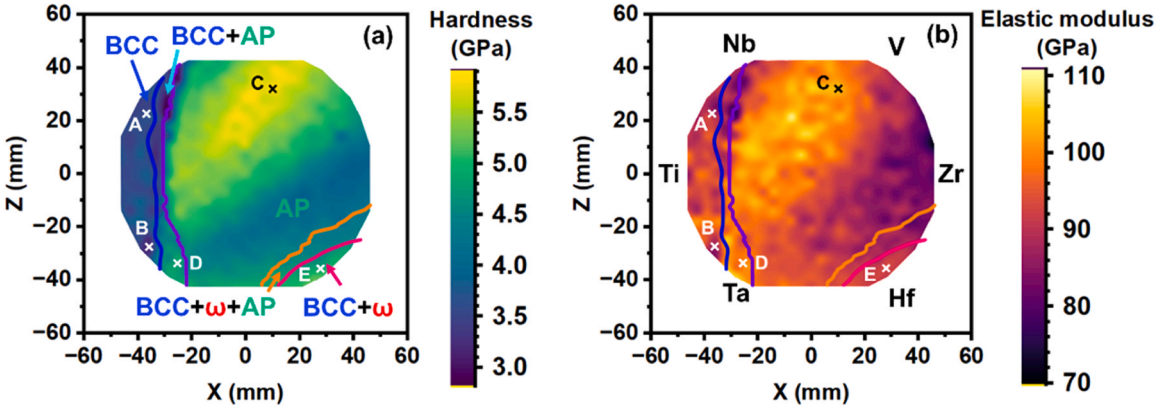

Fig. 4. (a) Hardness and (b) elastic modulus maps obtained by nanoindentation. The relative error of the hardness and modulus values was ± 4%. The curves indicate the boundaries of the regions with different phase contents. The crosses with capital letters indicate those 5 points where TEM study was carried out. The nanoindentation was performed in 574 positions. In the other points of the disk, the values were determined by interpolation and extrapolation.

an input parameter. As it was mentioned in Section 2.4, for all compositions $\nu = 0.4$ was assumed on the basis of the literature [26]. On the other hand, the value of the Poisson's ratio surely depends on the chemical composition. Former studies on the Hf-Nb-Ta-Ti-V-Zr composition space suggest that the Poisson's ratio varies in the range of 0.35–0.40 [27–30]. Thus, if the Poisson's ratio is 0.35 instead of the assumed value of 0.4 for some compositions in our combinatorial sample, the real elastic modulus is 5% larger than the value presented in this study. For the estimation of this error, the formulas of the Oliver-Pharr method was used. Since, for the studied compositions the elastic modulus varied between 76 and 111 GPa, the effect of the trends obtained in this study only marginally influenced by the uncertainty of the Poisson's ratio.

3.3. Study of the microstructure by XRD and TEM

For getting an impression on the variation of the XRD peak breadth in the Ta-Ti-Nb region, first the Full Width at Half Maximum (FWHM) mappings of peak 110 and 220 for all points in the Ta-Ti-Nb region are shown in Fig. S2 in the Supplementary material. It can be seen that the peak breadth decreases significantly from Nb target to Ta target, decreasing from 0.074 to 0.058 nm^{-1} in the case of peak 110, and from 0.124 and to 0.108 nm^{-1} for reflection 220, i.e., in the Ta-Ti-Nb region closer to the Nb target the XRD peaks are broader. This may be caused either by the higher dislocation density or the smaller crystallite size. In addition, the changing trends of peak breadth of these two peaks are the same, which is reflected in the color changes of the contour plot. Although the breadth of the peak profiles significantly exceeded the instrumental broadening, the exact values of the microstructural parameters cannot be determined by X-ray line profile analysis, due to the inhomogeneity of the element's distribution, which will be illustrated later by the analysis of the cross-sectional STEM-EDS concentration data.

Complementary TEM investigations of the microstructure were carried out in five selected points of the coating. These locations were tested by nanoindentation and are indicated by black crosses in Fig. 4 as well as denoted by the letters A–E. The coordinates of these five points are listed in Table S2 in the Supplementary material. Points A and B were selected close to the upper and lower ends of the BCC Ta-Ti-Nb region, i.e., close to the Nb and Ta targets, respectively. The FWHM analysis presented in the former paragraph suggested that their microstructure may be different. Moreover, location B has the lowest hardness value in the Ta-Ti-Nb region. Point C is related to the highest hardness values and can be found in the amorphous region. Location D is at the boundary between the BCC + AP phase region and the AP area. Finally, an additional point denoted by E was selected in the BCC + ω dual-phase region close to the Hf target. The chemical composition for the selected five points as obtained by XRF are listed in Table S3 in the Supplementary material**.** In addition, the hardness and modulus values obtained by nanoindentation for these five points are listed in Table S4 in the Supplementary material**.**

Former investigations on the combinatorial Co-Cr-Cu-Fe-Ni-Zn [22] and Co-Cr-Fe-Mo-Ni-W [23] layers processed by similar deposition methods have revealed considerable porosity. Therefore, in this study STEM micrographs were taken on the cross section at the five points in order to investigate the porosity in the layer. As an example, Fig. 5**a** shows the cross section of the film in point A. The dark lines in the HAADF micrograph correspond to long pore channels which aligned approximately parallel to the growing direction of the layer. This morphology suggests a columnar growth of the film during deposition. Fig. 5**b** shows the layer cross section for location B where the porosity was the second highest among the studied five points. To characterize the porosity distribution features, STEM-HAADF images were processed using Gabor filtering [31]. First, the original image was gray scaled and normalized to improve contrast. Then, a multi-directional Gabor filter was constructed, and the image was convolved to extract linear feature responses in different directions. By comparing the average response intensity of each direction, the dominant background direction was identified and removed, thereby suppressing matrix stripe interference. The responses of the remaining directions were superimposed and normalized and then binarized to extract pore regions. Finally, the porosity was quantitatively determined by statistically analyzing the percentage of pixels in the binary image. This segmentation resulted in the black and white images in Fig. 5**c** and **d** from the micrographs in Fig. 5**a** and **b**, respectively. The pore fraction values are 4.4% and 1.9% for points A and B, respectively (experimental absolute error: 0.1%), while for other three points the porosity is almost zero. It is emphasized that the present analysis carried out on the STEM images determined the area fraction of the pores which may differ from the volume fraction of the pores since the latter depends on the three-dimensional pore morphology.

Fig. 6**a** shows BF-TEM image on the cross-sectional microstructure in point A where XRD indicated a BCC structure. The electron diffraction patterns and the corresponding radial intensity distributions with indexed peaks are shown in Fig. 6**b**–**d** for the top, middle and bottom parts of the layer, respectively. The top and middle parts have a BCC structure while the bottom part shows a BCC + AP mixed phase. The grains are elongated vertically with an average length of 331 nm and an average width of 64 nm, while the subgrain size is around 25 nm as determined from the dark field (DF) image based on the BCC peak 110 in the SAED pattern shown in Fig. S3 in the Supplementary material (the size values are listed in Table S2).

The chemical composition of point A was mapped on the film cross-

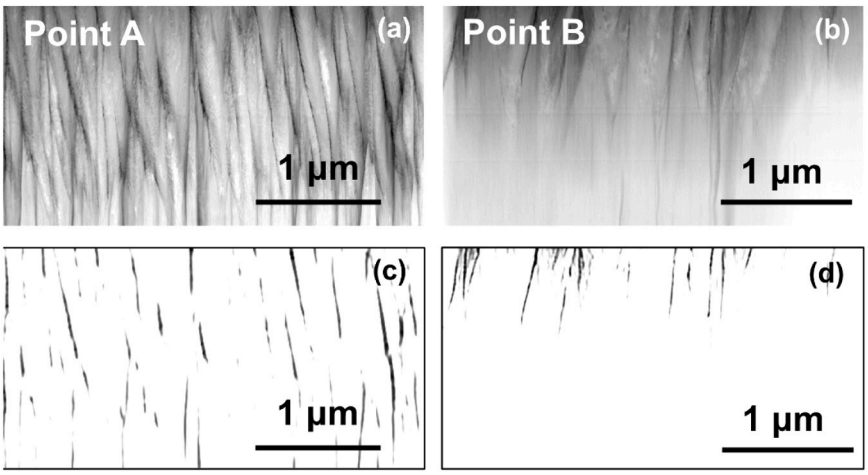

Fig. 5. STEM-HAADF micrographs taken on the cross section of the layer in the points (a) A and (b) B. The segmentation of the micrographs into material and pores was carried out by Gabor filter function and the resulted images for points A and B are shown in figures (c) and (d), respectively. The layer-normal direction is vertical.

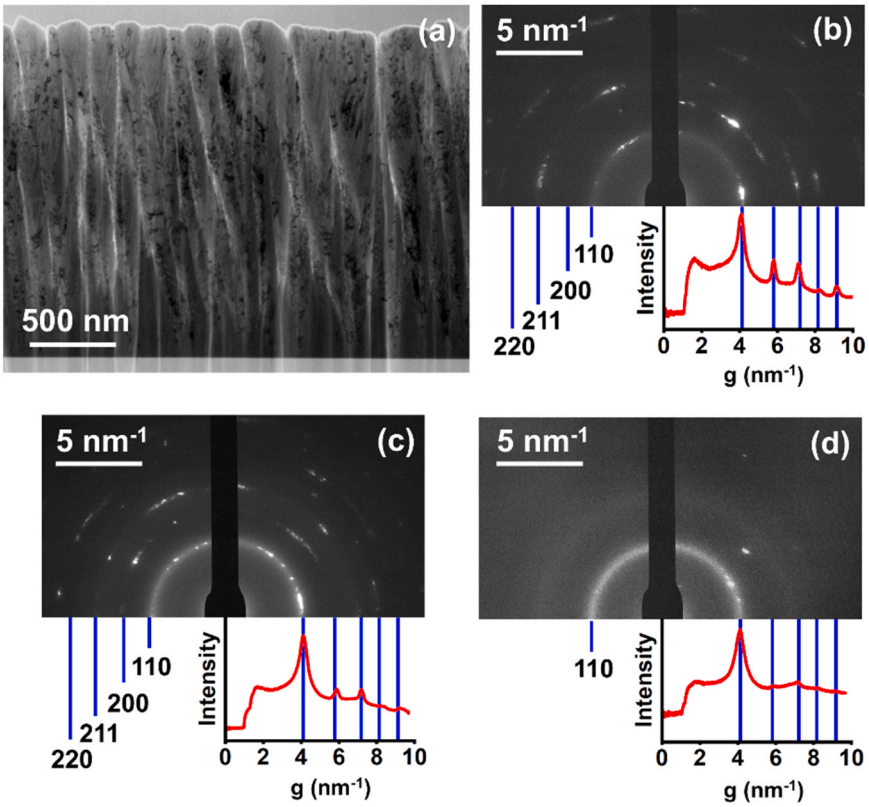

Fig. 6. (a) BF image taken on the cross-section in point A, the electron diffraction pattern and the corresponding radial intensity distribution with indexed peaks for (b) top, (c) middle and (d) bottom parts of the layer.

section using STEM-EDS, as shown in Fig. 7. The studied area can be seen in the HAADF micrograph in Fig. 7**a**. In the amorphous region at the bottom, the EDS image shows a relatively uniform elemental distribution. However, in the upper BCC region, the overall elemental distribution exhibits a non-uniform characteristic. There is no significant difference in the average elemental composition between the top and bottom regions. The comparison between Fig. 7**a** and **h** reveals that oxygen adheres to the surface of the pores. In addition, the element maps in Fig. 7 suggest chemical heterogeneities in the BCC region on the top of the layer. The analysis of the EDS data revealed that Ti varies complementary with the elements Zr, V and Hf, while Nb changes in a complementary way with Ta. As an example, the complementary variation of Ti and V is shown in Fig. 7**i**. It is noted that considerable difference between the chemical compositions in the top, middle and bottom one-thirds of the layer was not found by cross-sectional TEM-EDS. This is valid for all the five studied points.

Fig. 8**a** shows BF-TEM image on the cross-sectional microstructure in point B where XRD indicated a BCC structure. The electron diffraction patterns and the corresponding radial intensity distributions with indexed peaks are shown in Fig. 8**b-d**. The top and middle parts show BCC and BCC + AP structures, respectively, while the bottom part is an AP phase. The columns are growing like a tooth shape on the upper half

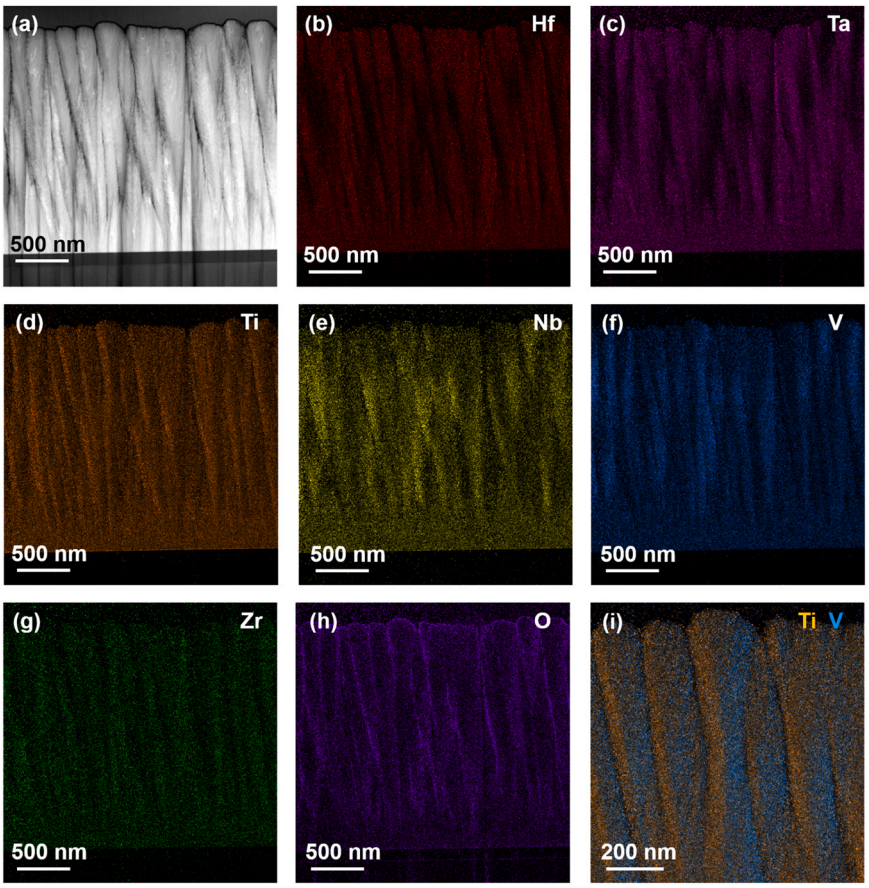

Fig. 7. (a) HAADF image taken in point A and the corresponding EDS elemental maps for (b) Hf, (c) Ta, (d) Ti, (e) Nb, (f) V, (g) Zr and (h) O. Combined EDS map for Ti and V in (i) illustrates the complementary element distribution at the two sides of the crystalline columns.

part of the coating, with an average grain length of 152 nm and an average grain width of 36 nm, the subgrain size is around 23 nm which were determined from the DF image based on peak 110 in the SAED pattern as shown in Fig. S4 in the Supplementary material.

A HAADF cross-sectional micrograph taken in point B is shown in Fig. 9**a**. The chemical composition of point B was mapped on the film cross-section using STEM-EDS, as shown in Fig. 9**b-h**. The overall distribution of elements exhibits homogeneous distribution on the lower part with amorphous structure, while the upper half part with BCC structure exhibits inhomogeneous element distribution. There is no significant difference in the average elemental composition between the top and bottom regions. Oxygen is attached to the surface of the pores as shown in Fig. 9**h**. The analysis of the EDS data revealed that in the upper part of the layer (BCC region) there are chemical heterogeneities. Namely, Ti varies complementary with Hf while the same can be observed for the pair Ta and Nb. As an example, Fig. 9**i** illustrates the spatial distribution for the element pair Nb and Ta.

Fig. 10**a** shows BF-TEM image on the cross-sectional microstructure in point C where XRD indicated an amorphous structure. The electron diffraction patterns and the corresponding radial intensity distributions taken on the top one-third of the layer are shown in Fig. 10**b** which reveals an amorphous structure. In position C, the whole layer exhibits the same structure. The film cross-section is also shown in the HAADF micrograph in Fig. S5a in the Supplementary material. The chemical composition of point C was mapped on the film cross-section using STEM-EDS, as shown in Fig. S5b-**h** in the Supplementary material. The overall distribution of elements is homogeneous with no visible porosity. Hence, the oxygen is attached on the surface of the coating only.

Fig. 11**a** shows BF-TEM image on the cross-sectional microstructure in point D where XRD indicated a BCC + AP structure. The electron diffraction patterns and the corresponding radial intensity distributions with indexed peaks taken on the top, middle and bottom parts of the coating are shown in Fig. 11**b-d**. The top and middle parts are both shown as BCC + AP structure while the bottom part shows a total AP phase. The grains are growing like a needle shape on the upper half part, with an average length of 126 nm and an average width of 30 nm, while the subgrain size is around 23 nm which are determined from DF image based on the BCC peak 110 on the SAED pattern, as shown in Fig. S6 in the Supplementary material. Thus, it seems that the BCC peaks in the XRD pattern taken in point D originate from the needle-like BCC grains embedded in an amorphous matrix.

The HAADF cross-sectional micrograph in Fig. S7a (see the Supplementary material) shows the film in point D. The chemical composition was mapped on the film cross-section using STEM-EDS, as shown in Fig. S7b-**h**. The overall distribution of elements is inhomogeneous in the upper half part with BCC structure. The lower part with amorphous structure exhibits homogeneous element distribution. The oxygen is attached on the surface of the pores which have a negligible fraction in point D compared to points A and B. The analysis of the EDS data revealed that in the upper part of the layer (BCC region) there are chemical heterogeneities. Namely, Ti varies complementary with Hf while the same can be observed for the pair Ta and Nb. The complementary pairs are the same as point B, since their positions are close to each other. The overall distribution of elements in the amorphous area is homogeneous with no visible porosity.

Fig. 12**a** shows BF-TEM image on the cross-sectional microstructure in point E where XRD indicated an BCC + ω structure. The electron diffraction patterns and the corresponding radial intensity distributions with indexed peaks for top, middle and bottom parts of the layer are shown in Fig. 12**b-d**. All of these three parts exhibit mainly BCC

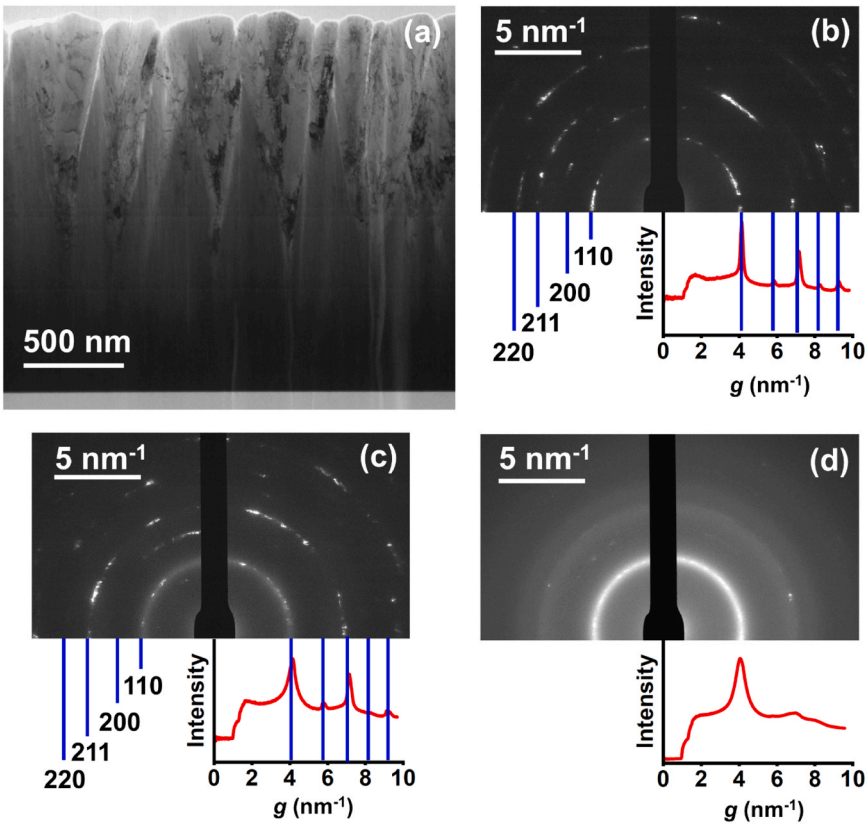

Fig. 8. (a) BF image taken on the cross-section in point B, as well as the SAED patterns and the corresponding radial intensity distributions with indexed peaks for (b) top, (c) middle and (d) bottom parts of the layer.

structure. The grains are uniformly distributed in the whole region with an average length of 98 nm and an average width of 18 nm, while the subgrain size is around 18 nm which are determined by the DF image based on the BCC peak 110 on the SAED pattern, as shown in Fig. S8 in the Supplementary material. A HAADF cross-sectional micrograph is shown in Fig. S9a in the Supplementary material. The chemical composition in point E was mapped on the film cross-section using STEM-EDS, as shown in Fig. S9b-**h**. The overall distribution of elements exhibits homogeneity without considerable porosity. Hence, the oxygen can be found only on the surface of the coating.

In general, the large grains can be found mostly on the top of the layer in point A (Fig. S3). This may be caused by the V-shape growing of the crystalline columns: closer to the substrate only small crystalline nuclei form while as the columns grow the width and the length of the grains inside the columns are higher. Since in points B and D the nucleation of the crystalline columns begins later than in point A during deposition as revealed by the thicker amorphous layer in the bottom of the film, only smaller crystalline grains can develop until the end of the deposition process. For point E, a dual phase crystalline microstructure forms and the grains of the two phases hinder the growth of each other, resulting in a relatively small grain size.

4. Discussion

4.1. Compositional dependence of the phase content and the lattice constant

The phase map shown in Fig. 2**a** is worth comparing with theoretical predictions. First, the three most commonly applied criteria for HEAs are checked. Fig. 13**a** shows the enthalpy of mixing (ΔH_{mix}) map calculated from the binary mixing enthalpies and the constituent concentrations using the following formula:

$$\Delta H_{mix} = \sum_{i<j} 4\Delta H_{ij}^{mix} c_i c_j \quad (1)$$

where ΔH_{ij}^{mix} represents the binary enthalpy of mixing between the i^{th} and j^{th} elements while c_i and c_j are their atomic concentrations [32,33]. For HEAs, the value of ΔH_{mix} should be between −15 and 5 kJ/mol [34]. In the present combinatorial sample, for all points (i.e., chemical compositions) ΔH_{mix} varies between −2.6 and 2.2 kJ/mol; therefore, this HEA condition is fulfilled. The second criterion studied here is related to the mixing entropy (ΔS_{mix}) that should be higher than $1.5 \times R$ for HEAs [35]. This quantity was calculated for each point of the combinatorial sample using the following formula:

$$\Delta S_{mix} = -R\sum_{i=1}^{n} c_i \ln c_i \quad (2)$$

where n is the number of constituent elements. Fig. 13**b** shows that for almost all points in the combinatorial disk the mixing entropy varies between $1.5 \times R$ and $1.75 \times R$; therefore, this condition is also fulfilled. A third, often cited criterion says that the absolute value of the ratio of the entropy and enthalpy terms in the Gibbs-free energy of mixing at the melting point should be higher than 1.1 [36]. This ratio is denoted as Ω and calculated as the absolute value of $T_m\Delta S_{mix}/\Delta H_{mix}$. The values of Ω are mapped in Fig. 13**c** for the present combinatorial sample, where the lowest value is 10, thus the Ω criterion for HEAs is fulfilled for all compositions present in this combinatorial disk.

For the formation of single phase crystalline structure, a fourth criterion should also be fulfilled which describes the atomic size differences between the constituent elements. Namely, the radii of the components must not be very different for forming a disordered crystalline solid solution. This criterion is represented by parameter δ which can be calculated as [35]:

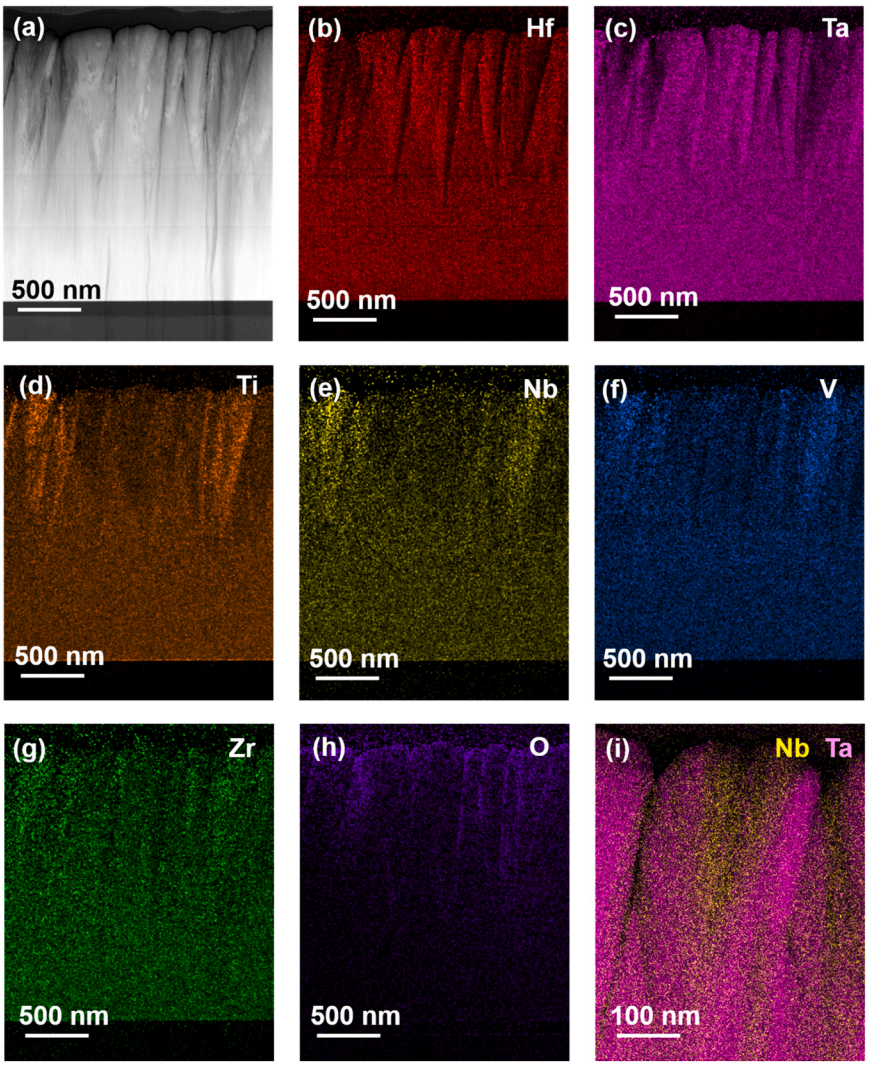

Fig. 9. a) HAADF image taken in point B and the corresponding EDS elemental maps for (b) Hf, (c) Ta, (d) Ti, (e) Nb, (f) V, (g) Zr and (h) O. The combined EDS map for Nb and Ta in (i) illustrates the complementary element distribution at the two sides of the crystalline columns.

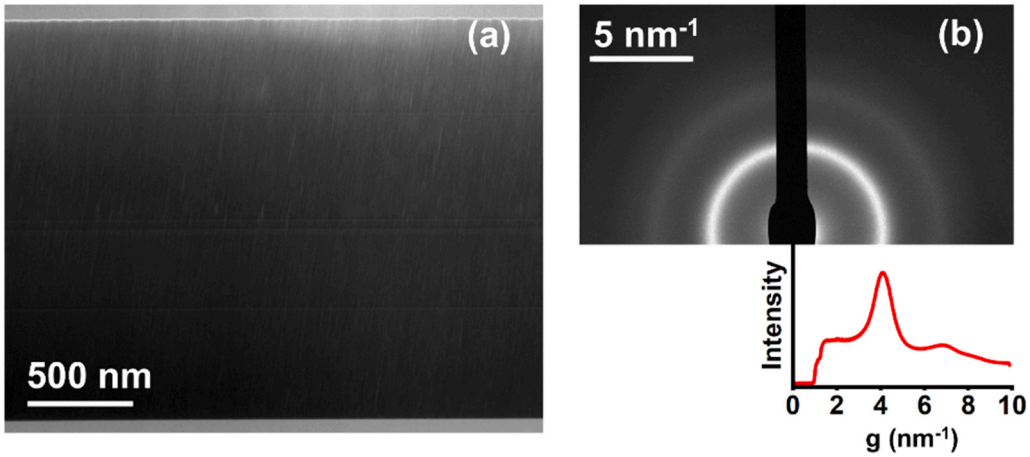

Fig. 10. (a) BF image taken on the cross-section in point C and (b) the electron diffraction pattern obtained on the top of the layer and the corresponding radial intensity distribution.

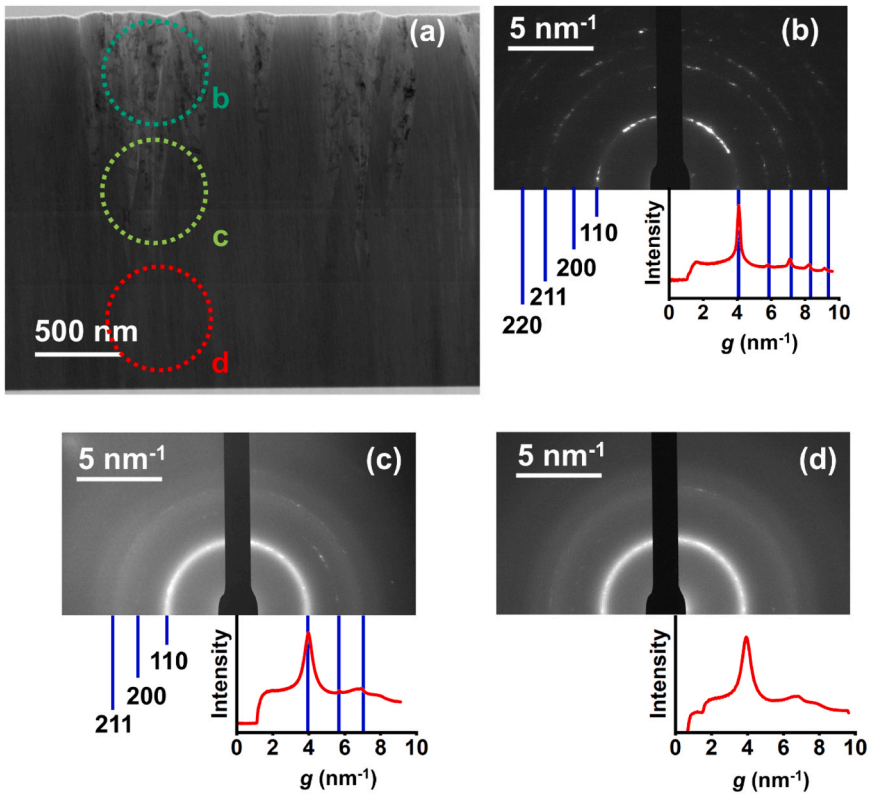

Fig. 11. (a) BF-TEM image taken on the cross-section in point D. The electron diffraction pattern and the corresponding radial intensity distribution with indexed peaks for (b) top, (c) middle and (d) bottom parts of the layer (the studied areas are indicated by dotted circles in (a)).

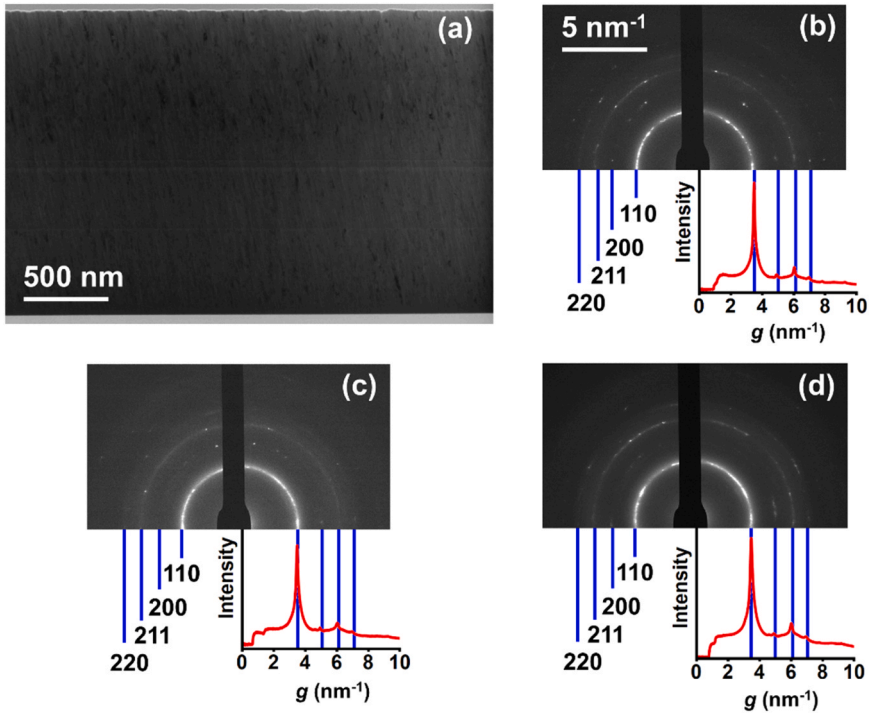

Fig. 12. (a) BF-TEM image taken on the cross-section in point E. The electron diffraction patterns and the corresponding radial intensity distributions with indexed peaks for (b) top, (c) middle and (d) bottom parts of the layer.

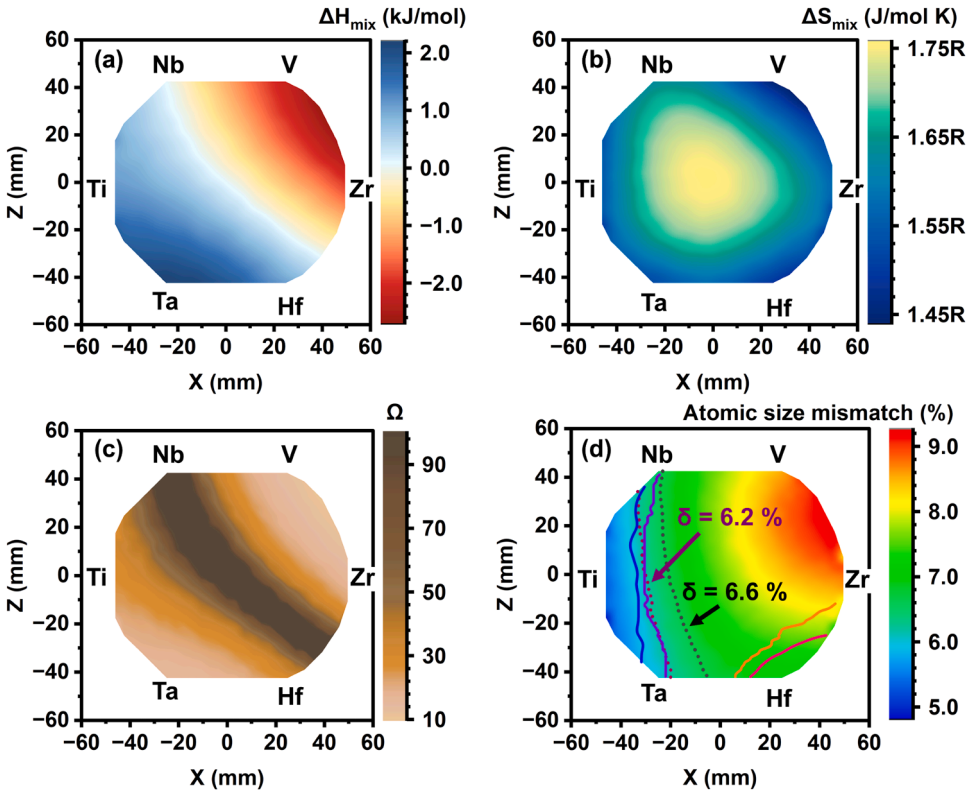

Fig. 13. Maps for (a) enthalpy of mixing (ΔH_{mix}), (b) entropy of mixing (ΔS_{mix}), (c) Ω parameter (calculated as the absolute value of $T_m\Delta S_{mix}/\Delta H_{mix}$ where T_m is the melting point) and (d) atomic size mismatch parameter (δ) calculated for the Hf-Nb-Ta-Ti-V-Zr combinatorial film.

$$\delta = \sqrt{\sum_{i=1}^{n} c_i\left(1-\frac{r_i}{\bar{r}}\right)^2} \tag{3}$$

where r_i is the atomic radius of the ith element and $\bar{r}$ is the average atomic radius of the alloy given as:

$$\bar{r} = \sum_{i=1}^{n} c_i r_i \tag{4}$$

Former studies have shown that the crystalline solid solution phases tend to form when δ < 6.6%. The map of the δ values for the present Hf-Ta-Ti-Nb-V-Zr combinatorial disk is shown in Fig. 13**d**. The criterion δ = 6.6% is represented by a dotted line which deviates from the boundary line separating the AP and the BCC + AP regions near the Ta/Ti/Nb targets. If the threshold value of δ is modified to 6.2%, a very good agreement is observed between the predicted and the experimental boundary of the AP region. Thus, for chemical compositions with δ> 6.2% amorphous and/or multiphase crystalline structures form in the Hf-Ta-Ti-Nb-V-Zr combinatorial sample, even if the other three HEA conditions for ΔH_{mix}, ΔS_{mix} and Ω are satisfied. However, there is uncertainty in identifying the amorphous/BCC phase boundary, thus the refined threshold (6.2%) is an approximate value.

For the disk points with δ values around the threshold (6.2%), a dual-phase BCC + AP structure forms. The present TEM experiments reveal that where crystalline and amorphous phases co-exist, the bottom part of the layer is mostly occupied by AP phase and the fraction of BCC phase increases when the surface of the coating is approached (see Fig. 8 and Fig. 11 for points B and D, respectively). This phenomenon can be explained by the following way. When the film growth starts on the substrate, the arriving atoms initially freeze into an amorphous structure due to the low temperature (RT) of the substrate and the amorphous structure of the SiN_x thin coating on the Si substrate which thus can not serve as a seed of crystalline grain formation. This effect is especially strong because the configurational complexity of a six-component alloy consisting of elements with very different sizes frustrates atomic ordering. As a result, the first deposited atoms can become kinetically trapped before they find energetically favorable lattice positions, producing an amorphous layer. The influence of substrate decreases with increasing film thickness. On the other hand, in the amorphous layer internal stresses and local chemical fluctuations may develop, which may create nanoscale crystalline nuclei. The formation of crystalline nuclei can release the stresses in their occupied volumes while the chemical fluctuations can yield small volumes where δ is smaller, which makes the material suitable for crystalline structure. After a stable BCC nucleus forms, continued growth becomes much easier because the new atoms can attach to an existing BCC lattice. During growing of the BCC columns, they form V-shaped regions which is typical for competitive growth [37–39].

It is worth noting that although the δ values are similar (around 6.0%) for points A, B and D, the AP contents in these points are different. Namely, while in point A considerable amount of amorphous structure was not detected, in points B and D the bottom part of the layer is mostly occupied by AP phase. This observation can be attributed to the different mobilities of the deposited atoms in the three places due to the various chemical compositions. Indeed, the atomic mobility depends on the homologous temperature which is determined by the chemical composition. An effective homologous temperature can be calculated as the ratio of the substrate temperature and the concentration-weighted average melting points of the constituent elements. The average melting temperatures for points A, B and D are 2089, 2299 and 2336 °C, respectively, thus in these points RT corresponds to the effective homologous temperatures of 0.127, 0.117 and 0.115. The lower homologous temperatures of deposition in points B and D yields a less ability of the adatoms to diffuse/rearrange into energetically favorable crystalline configuration during sputtering. As the deposition proceeds, the probability of nucleation of crystallites increased as discussed in the former

paragraph. The high average melting temperature in points B and D is caused by the large fraction of Ta which has a much higher melting temperature (3017 °C) than those of the other constituent elements (1668–2477 °C). The promoting effect of the high Ta content on the amorphization in Hf-Nb-Ta-Ti-Zr alloys has been shown in a former study for severely deformed samples [40]. During severe plastic deformation (SPD), the amorphization is usually caused by the extremely large atomic disorder associated with the high density of defects such as dislocations and grain boundaries. The lower effective homologous temperature in the locations with high Ta contents hinders the annihilation of defects formed during SPD, thereby promoting amorphization as shown in Ref. [40]. Thus, it can be concluded that beside the large δ value, which represents the thermodynamic reason of amorphization, the kinetic retardation of crystallization due to the low adatom mobility caused by the low homologous temperature of deposition also contributes to the formation of AP structure.

For single-phase HEAs, the crystal structure can be predicted from the valence electron concentration (VEC) [41].VEC is calculated as the average of the VEC values of the constituent elements weigthed with their atomic fractions. An empirical rule suggests that if VEC is lower than 6.9 BCC structure forms while above 8 the FCC phase is stable [42]. Between these two values, a dual-phase structure forms. In the present case, for all compositions the VEC is lower than 5 since the VEC is 4 for Hf, Ti and Zr, while 5 for Nb, Ta and V; therefore, this empirical rule suggests the development of a BCC major phase where crystalline structure forms, which is in accordance with the present experimental observation.

For the two crystalline regions close to the Ta/Ti/Nb and the Hf targets, the lattice constant map of the BCC major phase was determined by XRD and plotted in Fig. 3. For the single phase BCC area near the Ta/Ti/Nb targets, the lattice constant reaches its maximum value near the Ta target and decreases gradually toward the Nb target. This trend can be related to the different atomic radii of the constituent elements. This effect is illustrated in Fig. 14**a**, where the spatial distribution of the average atomic radius on the combinatorial disk surface is mapped. The average atomic radius on the whole disk surface varies between 140.2 ± 0.6 pm and 152.4 ± 0.6 pm. In the single phase BCC region near the Ta/Ti/Nb targets, it changes to a narrower range between 143.4 ± 0.6 pm and 145.9 ± 0.6 pm. For studying a possible correlation between the lattice constants and the constituent elements sizes, the lattice parameter values measured for the BCC phase in the regions close to the Ta/Ti/Nb targets are plotted as a function of the average atomic radius in Fig. 14**b**. In this analysis, for each XRF measurement location we selected the closest XRD measurement point in order to maximize the reliability of the comparison between the calculated average atomic radius and the experimentally determined lattice constant. The correlation observed between the two quantities suggests that the lattice constant variation in the BCC phase is caused by the variation of the fractions of the small and large elements. On the other hand, in the crystalline region close to the Hf target the lattice parameter remains unchanged (about 0.3470 nm) within the experimental error even if the chemical composition changes. This effect is in accordance with the slight variation of the average atomic radius (between 150 and 151 pm). It should be noted, however, that the chemical composition of the main BCC phase may deviate from the average composition due to the formation of the secondary ω phase [43]. Thus, the real average atomic radius in the BCC phase may deviate from the values calculated from the average element concentrations. However, this deviation should be low due to the small fraction of the ω phase.

Fig. 7**i** and Fig. 9**i** reveal that the various parts of the BCC columns have significantly different element concentrations. For instance, in point A the concentration of element Ti varies complementary with those of Zr, V and Hf, and the same was observed for the element pair of Nb and Ta. Accordingly, Fig. 4**b** shows that targets Hf/V/Zr are located on the opposite side of the disk from Ti target and the same is valid for Nb and Ta targets. Thus, in point A the atoms sputtered from the opposite targets arrive to the substrate from different directions. If we consider that the target-substrate spacing is low [44] and the top of the growing BCC columns is curved (see Fig. 7**a**), the complementary composition distribution in the two sides of the columns can be explained by the "shadowing effect" illustrated in Fig. 15. Namely, on the side farther from the given target, the corresponding element deposition is less probable due to the shadow made by the column. For instance, in point A elements Ti and V have complementary concentration distributions as shown in Fig. 7**i**. Fig. 15**a** and Fig. 15**b** present, respectively, the top and side views of the substrate disk and the Ti and V targets. Considering the relative positions of the targets and point A in the deposited layer, it can be calculated that the growing columns can be seen from the targets under the angle of 30–40° The resulted elemental inhomogeneity in the column is illustrated in the inset of Fig. 15**b** where the blue and red colors correspond to elements V and Ti, respectively. This complementary element distribution resembles to the experimental result shown in Fig. 7**i**. It should be noted that in the TEM images the growing direction is pointing up while in the sputtering chamber (and also in Fig. 15) it is pointing down in accordance with the real sputter-up arrangement. It is also worth noting that the concentration distribution in the columns depends on the position of the column on the substrate disk, the growing direction of the column relative to the substrate normal and the shape of the cap. Thus, the inset in Fig. 15**b** illustrates only a case which is close to the reality but it is not valid generally.

For the amorphous structure in point C, the surface remains flat during growing as shown in Fig. 10**a**, thus chemical heterogeneities were not observed (see Fig. S5 in the Supplementary material). It is noted that the dome-like shape of the top of the growing crystalline

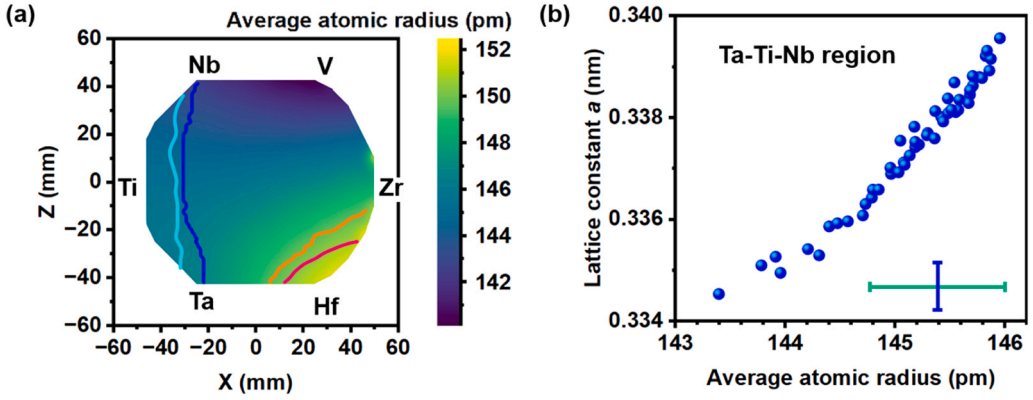

Fig. 14. (a) Map of the calculated average atomic radius for the studied Hf-Ta-Ti-Nb-V-Zr combinatorial disk. The error of the calculated average atomic radius is ± 0.6 pm. (b) The experimentally determined lattice parameter of the BCC phase versus the calculated average atomic radius in the single BCC phase region close to the Ta/Ti/Nb targets. The error bars in (b) can be seen in the corner of the figure.

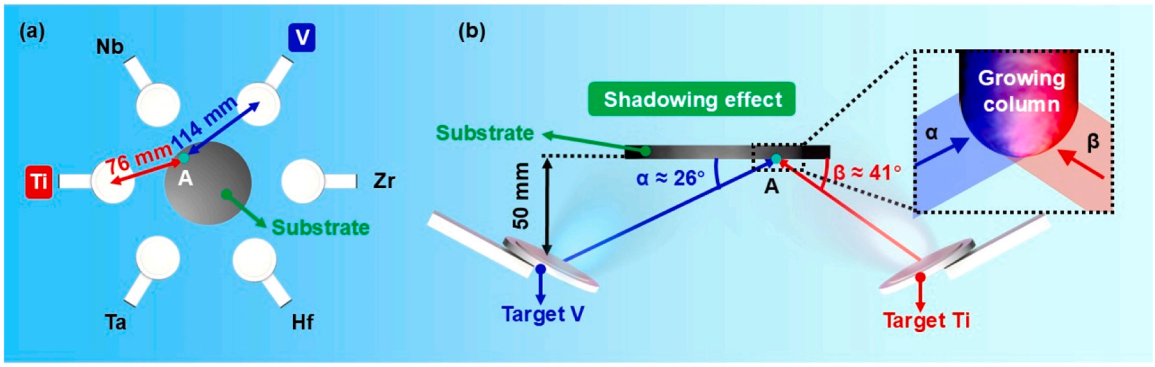

Fig. 15. Schematic showing the shadowing effect during magnetron sputtering in point A when due to the curved caps of the growing crystalline columns their left and right sides have complementary element concentrations. (a) Top view of the substrate disk and the six targets. The distances between point A and the centers of the Ti and V targets projected onto the plane of the substrate disk are also shown. (b) Side view of Ti and V targets and the substrate disk where the blue and red lines with arrows represent the V and Ti atomic flux towards point A. The inset in (b) shows a growing crystalline column with dome-like shape cap, resulting in complementary element concentrations at the left and right sides.

columns is not a unique feature of these HEA compositions. This effect has already been observed for other alloys or even pure metals deposited in the form of thin films [45]. When dome-shaped caps formed between grain boundaries intersecting the growing surface, the surface curvature can be explained by the difference between the grain boundary and surface energies [38]. Moreover, since sputtering occurred at low homologous temperature (at RT), the surface diffusion is very slow; therefore, small surface height differences cannot be smoothed. Rather, regions behind or beside the protrusion receive slightly less flux because they are geometrically screened (shadowing effect), thus the height fluctuation amplifies with increasing deposition time, yielding dome-shaped column caps.

4.2. *X-ray diffraction peak broadening caused by chemical heterogeneities*

Fig. 2**c and d** show that the XRD peaks of the BCC phase have a considerable broadening. In former studies on other combinatorial HEA samples, the XRD peaks obtained by synchrotron radiation were evaluated by X-ray line profile analysis (XLPA) for the crystallite size and the density of lattice defects such as dislocations and twin faults [23,46–48]. A detailed description of XLPA can be found in Ref. [49]. On the other hand, in the present case the BCC phase columns exhibit a chemical heterogeneity which also contributes to XRD peak broadening. This latter effect was estimated from the concentration distribution and compared with the experimentally observed peak broadening in order to decide whether the crystallite size and the dislocations density are worth determining by XLPA. This estimation procedure for points A and B is depicted in the next paragraphs.

In point A, the variation of the chemical composition was determined along a line with the length of 460 nm on the film cross-section as shown by the red dotted rectangle in HAADF image in Fig. 16**a**. The corresponding atomic fractions along the line are presented in Fig. 16**b**. The fraction data were smoothed by locally weighted scatterplot smoothing (lowess) by using only the nearest 10% of data points to estimate each smoothed value. The smoothed concentration distributions for all elements are shown by the noise-free solid curves in Fig. 16**b**. In the next step, the spatial distribution of the average atomic radius is determined from the smoothed concentration values and the atomic radii of the constituent elements (the latter values are listed at the end of Section 3.1). The variation of the average atomic radius is plotted in Fig. 16**c**. The range of the local atomic radius variation is about 3 pm which corresponds to ±1% relative variation around the spatial average. The change of the atomic radius from point to point yields a proportional variation of the local interplanar spacing in the BCC structure. This leads to a variation of the position of the diffraction peak components scattered from the different points of the BCC phase in accordance with the Bragg's law. The shift of the position of the XRD peak component scattered from a certain position can be quantitatively related to the deviation of the local atomic radius (r_{loc}) from the spatially averaged value using the Bragg's law. By differentiating the Bragg's equation, the variation of the interplanar spacing (Δd) is related to the angular shift of the diffraction peak ($\Delta(2\theta)^\circ$) as:

$$\Delta(2\theta)^\circ \approx \left[2\tan\theta \bullet \frac{\Delta d}{d}\right] \times \frac{180}{\pi} \tag{5}$$

where d is the interplanar spacing and θ is the Bragg angle. Using the

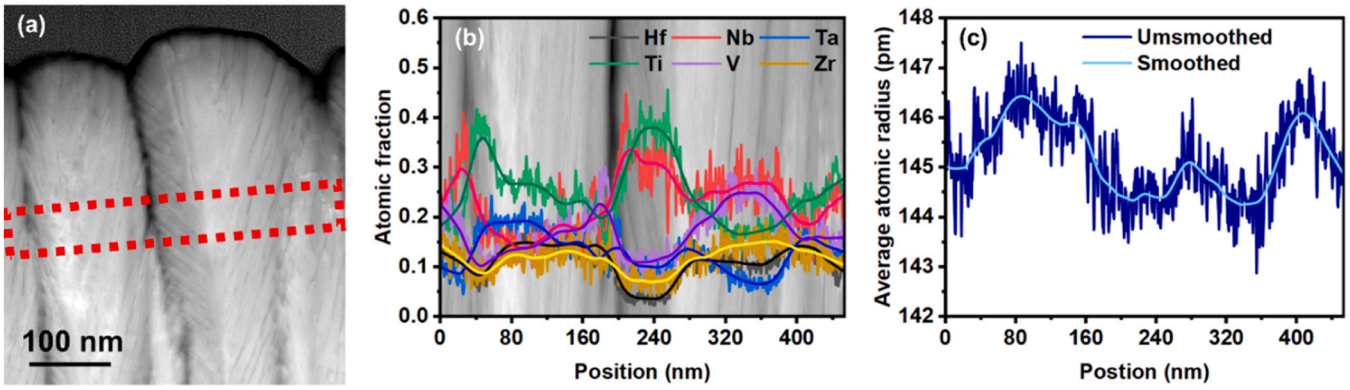

Fig. 16. (a) HAADF image taken at point A. (b) The atomic fractions of the six constituent elements and (c) the corresponding average atomic radius along the red dotted rectangle in (a).

assumed proportionality between the interplanar spacing and the local atomic radius, the deviation of r_{loc} from the spatially averaged value (Δr_{loc}) yields the following $\Delta(2\theta)^{\circ}$:

$$\Delta(2\theta)^{\circ} \approx \left[2\tan\theta \bullet \frac{\Delta r_{loc}}{r_{loc}}\right] \times \frac{180}{\pi}. \quad (6)$$

Using this formula, a histogram of $\Delta(2\theta)^{\circ}$ was determined from the distribution of r_{loc} and plotted for the first five peaks of the BCC phase in point A as shown in Fig. S10 in the Supplementary material. This figure also shows the experimentally determined peak profiles as solid lines. For these peaks, first the background was removed, and their peak centers were determined by fitting Pseudo-Voigt functions. These peak centers were set as reference points ($\Delta 2\theta = 0^{\circ}$). The comparison of the experimentally determined peak profiles and the calculated histograms reveals that the chemical heterogeneity effect gives the vast majority of peak broadening. Therefore, the microstructural parameters (crystallite size and dislocation density) in point A cannot be determined by XLPA.

For point B, the spatial change of the atomic fractions of the six elements and the corresponding variation of the local atomic radius are shown in Fig. 17. The calculated XRD peak component distributions for the first five peaks of the BCC phase are shown as histograms in Fig. S11 in the Supplementary material. The comparison of the experimentally determined peak profiles and the calculated histograms reveals that the chemical heterogeneity effect gives the vast majority of peak broadening. Therefore, the microstructural parameters (crystallite size and dislocation density) in point B cannot be determined by XLPA similar to point A. It is noted that the EDS evaluation software requires the TEM sample thickness as an input parameter for the calculation of absorption correction for the element concentrations, the deviation of real thickness from the assumed value can yield an error in the chemical composition determined by TEM-EDS. For checking the effect of the TEM foil thickness on the concentration values, we evaluated the chemical composition for a representative area in point A by changing the TEM lamella thickness with a factor of four from 20 to 80 nm. It was found that the corresponding change in the atomic concentrations was only a few tenths of a percent for all the six elements which is within the experimental error of EDS. Thus, it can be concluded that the concentration fluctuations plotted in Figs. 16 and 17 are real effects and not influenced significantly even if the TEM foil thickness may change in the studied region.

4.3. Correlation between the microstructure and the mechanical behavior

The hardness varied between 2.8 ± 0.2 and 5.9 ± 0.3 GPa in the currently studied Hf-Ta-Ti-Nb-V-Zr combinatorial disk. The highest hardness was observed in the AP region near the V target where the chemical composition is 11.4% Hf – 7.9% Ta – 13.4% Ti – 13.8% Nb – 40.3% V – 13.2% Zr. This hardness value (5.9 ± 0.3 GPa) is almost the same as that obtained for the five-component equimolar Hf-Nb-Ti-V-Zr combinatorial film with amorphous structure reported by Fritze and co-workers, which shows a hardness of 6.5 ± 0.3 GPa [50]. The significant variation of hardness on the surface of the present combinatorial Hf-Ta-Ti-Nb-V-Zr disk can be attributed to the difference in chemical and phase compositions. All the three phases observed in the combinatorial sample are regarded as hard structures. In the BCC region close to Ti/Ta/Nb targets, the glide of screw dislocations is difficult due to their highly dissociated core [51–53]. In addition, this part of the layer has nanostructure which also increases the hardness. In the BCC + ω region close to the Hf target, the precipitated ω phase can hinder dislocation movement at interfaces, thereby achieving hardness enhancement. The relatively high hardness of the amorphous phase may be attributed to the absence of conventional dislocation-mediated plasticity. Indeed, it was found generally that amorphous alloys have higher strength (hardness) than their crystalline counterparts with the same or similar compositions as shown in the review article of Inoue [54]. This behavior can be attributed to the absence of readily gliding dislocations in the amorphous state of materials. Therefore, it is not surprising that in the present combinatorial disk the points with higher hardness values were found in the amorphous region of the layer.

Since most of the studied points are related to region AP, a more detailed analysis of the mechanical performance is carried out on the amorphous structures. In a metallic glass, plasticity occurs through shear transformation zones (STZs). STZ is a small atomic cluster in which the positions of atoms are rearranged during deformation [55–57]. The resistance of amorphous alloys against plastic deformation (i.e., the hardness) is influenced by the stiffness of the atomic bonds since a higher bond stiffness yields a more difficult rearrangement of atoms. Since the higher bond stiffness also increases the elastic modulus, it has been found that within a given metallic glass family (the basic constituents are the same) the hardness is proportional to the elastic modulus [58–60]. Therefore, for the present combinatorial sample the hardness versus modulus data obtained by nanoindentation in the AP region are plotted in Fig. 18**a**. In this figure, the data for the BCC and the BCC + ω regions are also plotted for comparison. For the amorphous structures, the hardness tends to increase with the elastic modulus, although a significant scattering of the points is evident. For the single phase BCC region close to Ti/Ta/Nb targets, the hardness is lower than that in the area AP. This may be explained with the porosity (see Fig. 5) and the dislocation-mediated plasticity in crystalline structures which requires less stress than the plastic deformation in amorphous materials. However, the porosity effect seems to be less pronounced since the elastic modulus in the BCC region is not very different from the values measured in the amorphous area and this parameter is also sensitive to porosity. Since the effect of porosity on the elastic modulus and the hardness depends on the volume fraction and the three-dimensional morphology of the pores, the two-dimensional pore fraction available

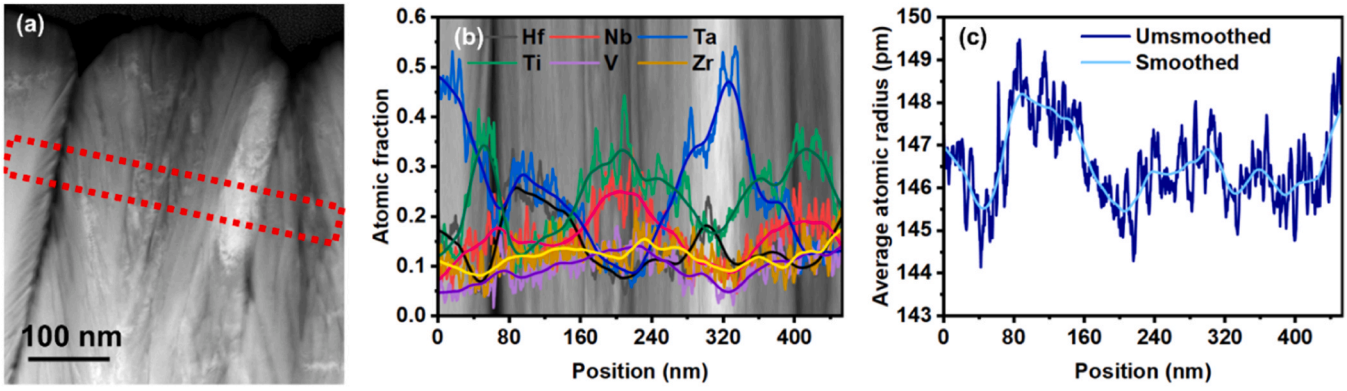

Fig. 17. (a) HAADF image taken at point B. (b) The atomic fractions of the six constituent elements and (c) the corresponding local atomic radius variation along the red dotted rectangle in (a).

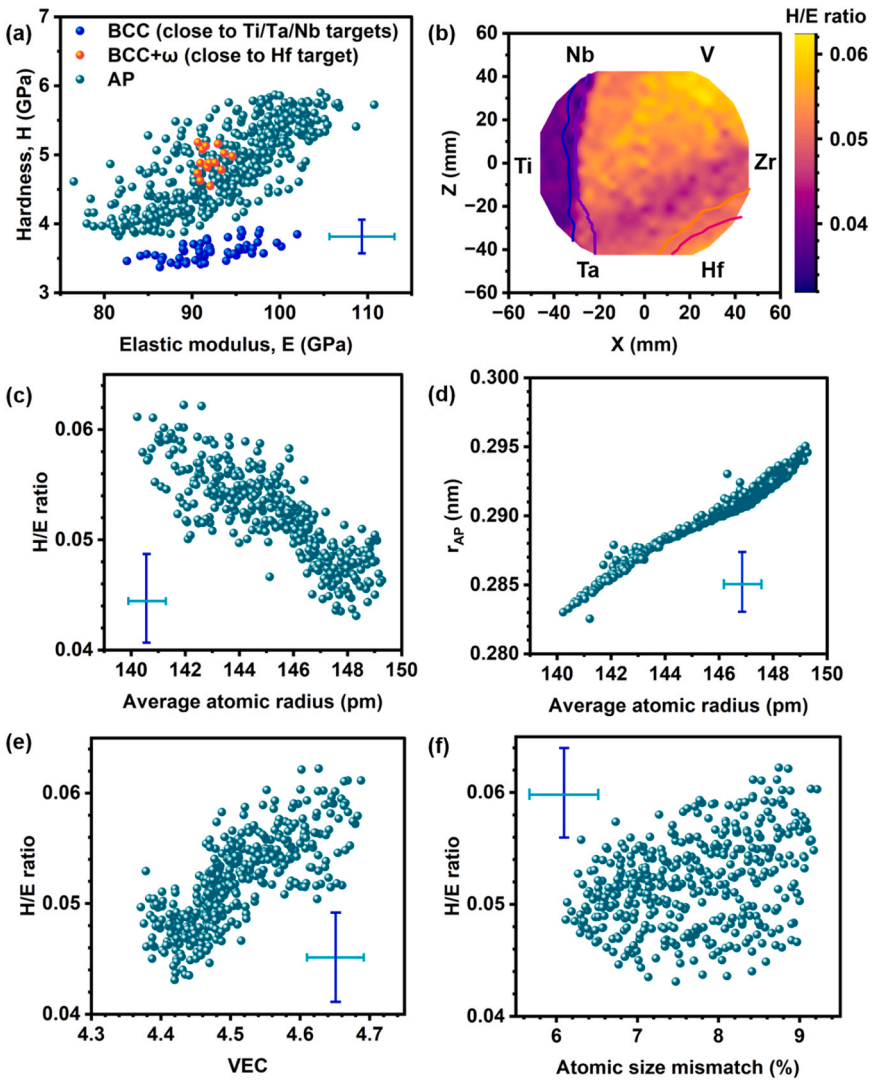

Fig. 18. (a) The hardness (H) versus the elastic modulus (E) obtained by nanoindentation for all tested points except the transient regions between the crystalline and amorphous areas. (b) The hardness over elastic modulus mapping. The H/E ratio versus (c) the average atomic radius for the tested points in the amorphous region. (d) The experimentally determined nearest-neighbor distance (r_{AP}) versus the calculated average atomic radius for the tested points in the amorphous region. The H/E ratio versus (e) the VEC values and (f) atomic size mismatch for the tested points in the amorphous region. The errors of the data are shown in the corners of the figures.

in this study is not suitable for a qualitative determination of the corresponding change of the mechanical properties. Nevertheless, the porosity effect should be low due to the small values of the area-fraction of pores (not higher than 4.4%). Despite the crystalline structure, the BCC + ω region exhibits hardness lying in the trend characteristic to the amorphous structures which can be explained by the strengthening effect of the ω secondary phase particles.

Since most of the studied compositions have an amorphous structure, the compositional dependence of the hardness is analyzed only in region AP. The scattering of the hardness versus modulus data in Fig. 18**a** suggests that beside the bond stiffness (represented by the modulus) other parameters also influence the hardness. For instance, the higher bond strength or packing density of atoms can also hinder plasticity via retarding the atomic rearrangements in STZs. For studying these effects, first the ratio H/E is mapped on the disk surface (see Fig. 18**b**) for revealing its dependence on the chemical composition. It is evident that H/E is the highest in the area close to the V target. Since V is the smallest element (atomic radius is 130 pm while for the other elements this value is between 142 and 160 pm), the average atomic radius has low values in the area close to the V target as shown in Fig. 14**a**. The effect of the average atomic radius on the hardness is reasonable since its low value must correspond to shorter bond length which yields stronger bonds, resulting in a higher hardness. Thus, the ratio H/E is plotted as a function of the average atomic radius for the amorphous points in Fig. 18**c**. Indeed, the lower atomic radius is mostly associated with a higher H/E ratio in this figure. The moderate scattering of the data can be attributed to the error of the values shown in the corner of the graph. Fig. 18**d** proves that the average atomic radius strictly determines the nearest-neighbor distance in the amorphous points. The latter quantity was determined from the position of the first diffuse peak (amorphous halo) of the XRD pattern. Thus, for the amorphous points the average nearest-neighbor distance (r_{AP}) was determined as $r_{AP}= 1.23/g$ where g is the magnitude of the diffraction vector ($g=2\sin\theta/\lambda$, λ is the wavelength of X-rays) for the first diffuse peak [61,62]. The peak position of the first XRD peak of the amorphous structure was determined by fitting Pseudo-Voigt function on the intensity profile within the 2θ range of 4.5–7.3°.

The strength of the atomic bonds may also be influenced by the average VEC value. Bonding in transition-metal metallic glasses is dominated by interactions involving d-electrons. A higher VEC value strengthens metallic bonding through enhanced d-orbital interactions.

Thus, H/E is plotted as a function of the average VEC in Fig. 18**e**. This figure suggests that the higher VEC basically yields a larger H/E ratio, although the scattering of the data is a bit higher than for the H/E versus average atomic radius relationship (see Fig. 18**c**). It is worth noting that in the studied compositional library, both the higher VEC and the lower atomic radius are related to the same elements: Nb, Ta and V. Thus, it is hard to decide which is the dominant in the determination of the H/E ratio. However, the atomic radius effect is more pronounced since in the vicinity of the V target the H/E is higher than close to Nb and Ta, and the VEC is the same for these three elements while the atomic radius is much smaller for V.

The present results suggest that the addition of V in this refractory compositional library is beneficial from the point of view of the mechanical performance. It is noted that beside the average atomic radius and VEC, other parameters (e.g., ΔH_{mix}, ΔS_{mix}, Ω or δ) have no reasonable correlation with the ratio H/E. As an example, Fig. 18**f** shows H/E versus the atomic size mismatch, δ. The higher value of δ usually corresponds to a higher packing density in the amorphous structure since the smaller atoms can occupy interstitial-like sites between the larger atoms. The lack of correlation between H/E and δ suggests that the packing density differences in the present combinatorial disk have no considerable effect on the hardness variation in region AP. Thus, the conclusion of the analysis presented above is that the hardness of the amorphous structures in the Hf-Nb-Ta-Ti-V-Zr compositional library is mainly determined by the strength of the atomic bonds, reflected in the average atomic radius. If we consider the whole compositional space including both amorphous and crystalline structures, the atomic size mismatch has also a deterministic effect on the hardness since the hard compositions exhibited high value of parameter δ (amorphous and multiphase structures). Therefore, the hardness is plotted as a function of δ and the average atomic radius for the whole compositional library in Fig. 19. Indeed, it can be concluded that the highest hardness values in the Hf-Nb-Ta-Ti-V-Zr system was achieved when high δ and low average atomic radius coexist.

It should be noted that the maximum hardness obtained for the amorphous structures in the present Hf-Nb-Ta-Ti-V-Zr combinatorial layer (5.9 ± 0.3 GPa) is not exceptional, considering former hardness results on thin film refractory metallic glasses in other compositional libraries. Since the hardness depends on the applied load (called as indentation size effect), the present maximum hardness obtained at the load of 6–8 mN can be compared only with values determined under similar condition. Therefore, only those hardness values were collected from the literature which were obtained at the maximum load between 5 and 10 mN. The hardness of these thin film refractory metallic glasses varied between 5.7 and 8.0 Gpa [63–67]. These former nanoindentation studies on other thin film refractory metallic glasses also reported that the elastic moduli fell within the range of 100–130 GPa, which overlaps with the range obtained in the present work (76–111 GPa). The difference between the mechanical properties of the presently studied Hf-Nb-Ta-Ti-V-Zr metallic glasses and the amorphous films formed in other compositional libraries may be attributed to the different layer deposition conditions and the various constituent elements. Indeed, it has been shown that the hardness and the elastic modulus of sputtered amorphous layers are significantly influenced by contaminants originating from the target and the chamber atmosphere [68]. Moreover, the atomic bond strength depends on the type of the constituent elements, which may also contribute to the difference between the mechanical properties of the presently studied thin film metallic glasses and the amorphous films formed in other compositional libraries.

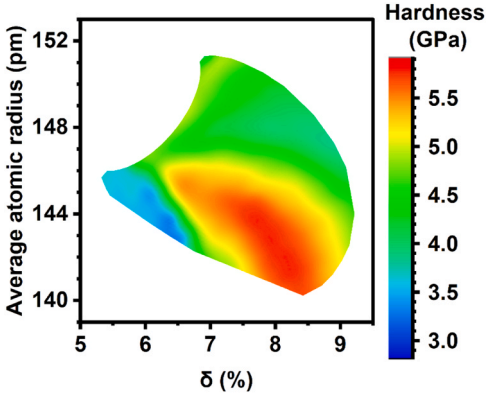

Fig. 19. The hardness as a function of δ and the average atomic radius for the whole Hf-Nb-Ta-Ti-V-Zr compositional library investigated in this study (including both amorphous and crystalline structures). The values between the tested points in the map were determined by interpolation using the Renka-Cline interpolation method in Origin software (Supplier: OriginLab Co., Northampton, USA).

It is also worth noting that the present study does not provide a complete mapping of the phase composition and the mechanical behavior in the Hf-Ta-Ti-Nb-V-Zr compositional library since the results were obtained for a certain arrangement of the pure element sources (targets). For instance, compositions having high concentrations for the oppositely placed target materials (e.g., Zr and Nb) cannot be found in the present combinatorial disk. Therefore, for a complete characterization of the Hf-Ta-Ti-Nb-V-Zr compositional library additional disks with different target arrangements are needed to be processed and analyzed. This will be a topic of a future work.

5. Conclusions

The Hf-Nb-Ta-Ti-V-Zr compositional library was studied experimentally for mapping the structure and mechanical performance of novel HEAs and metallic glasses. The investigated material was processed in the form of a layer with a thickness of about 2 μm using magnetron sputtering. The concentrations of the different elements span a wide range from 3–7% to 26–52%. The following results were obtained:

1. The majority of the studied compositions (80%) exhibited amorphous structures due to the large atomic size mismatch. It was found that for chemical compositions with δ> 6.2% amorphous and/or multiphase crystalline structures formed, even if the other three HEA conditions for ΔH_{mix}, ΔS_{mix} and Ω were satisfied. Single phase BCC structure developed only in the vicinity of the Ti/Ta/Nb targets while BCC matrix with an ω secondary phase formed close to the Hf target. In the transition regions, the lower part of the layer was amorphous while the upper parts contained crystalline columns. The lattice constant of the BCC phase correlated well with the average atomic radius.
2. The crystalline columns in the BCC region close to the Ti/Ta/Nb targets have dome-shaped caps and exhibited chemical heterogeneities which were caused by the shadowing effect. Namely, on the side farther from the given target, the corresponding element deposition is less probable due to the shadow made by the column. Thus, Ti varies complementary with the elements Zr, V and Hf, while Nb changes in a complementary way with Ta. It was found that most of the XRD peak broadening was caused by chemical heterogeneities.
3. The hardness varied between 2.8 ± 0.2 and 5.9 ± 0.3 GPa. The highest hardness was observed in the amorphous region close to the V target where the chemical composition is 11.4% Hf – 7.9% Ta – 13.4% Ti – 13.8% Nb – 40.3% V – 13.2% Zr. In general, the hardness of the amorphous points in the layer was larger than in the crystalline regions due to the lack of dislocations. The ratio H/E in the amorphous region was found to increase with increasing VEC and decreasing average atomic radius due to the increase in bond strength. Since element V has the lowest atomic radius and the highest VEC among the six constituents, the addition of V in this

refractory compositional library is beneficial from the mechanical performance point of view.

CRediT authorship contribution statement

Ao Wang: Writing – original draft, Visualization, Investigation. **László Pethö:** Writing – review & editing, Investigation, Formal analysis, Data curation, Conceptualization. **Zoltán Hegedűs:** Writing – review & editing, Investigation, Data curation. **Maria Wątroba:** Writing – review & editing, Investigation, Data curation. **Jorge de Oliveira:** Writing – review & editing, Investigation, Data curation. **Zsolt Czigány:** Writing – review & editing, Investigation, Data curation. **Johann Michler:** Writing – review & editing, Validation, Formal analysis. **Jenő Gubicza:** Writing – original draft, Validation, Supervision, Formal analysis, Conceptualization.

Ethical approval

Not Applicable.

Declaration of Competing Interest

The authors declare that they have no known competing financial interests or personal relationships that could have appeared to influence the work reported in this paper.

Acknowledgements

The authors thank Peter Denninger and Iuliia Baranova for their contribution to XRF measurements. We acknowledge DESY (Hamburg, Germany), a member of the Helmholtz Association HGF, for the provision of experimental facilities. Parts of this research were carried out at beamline P21.2. JG acknowledges the support by the National Research, Development and Innovation Fund of Hungary under project No. NKFIH-ADVANCED-153100. This research was supported by the grant no. VEKOP-2.3.3–15–2016–00002 and VEKOP-2.3.2–16–2016–00011 of the European Structural and Investment Funds.

Appendix A. Supporting information

Supplementary data associated with this article can be found in the online version at doi:10.1016/j.jallcom.2026.190804.

Data availability

Data will be made available on request.

References

[1] M.-H. Tsai, J.-W. Yeh, High-entropy alloys: a critical review, Mater. Res. Lett. 2 (2014) 107–123, https://doi.org/10.1080/21663831.2014.912690.
[2] E.J. Pickering, N.G. Jones, High-entropy alloys: a critical assessment of their founding principles and future prospects, Int. Mater. Rev. 61 (2016) 183–202, https://doi.org/10.1080/09506608.2016.1180020.
[3] D.B. Miracle, O.N. Senkov, A critical review of high entropy alloys and related concepts, Acta Mater. 122 (2017) 448–511, https://doi.org/10.1016/j.actamat.2016.08.081.
[4] E.P. George, D. Raabe, R.O. Ritchie, High-entropy alloys, Nat. Rev. Mater. 4 (2019) 515–534, https://doi.org/10.1038/s41578-019-0121-4.
[5] G.A. Salishchev, M.A. Tikhonovsky, D.G. Shaysultanov, N.D. Stepanov, A. V. Kuznetsov, I.V. Kolodiy, A.S. Tortika, O.N. Senkov, Effect of Mn and V on structure and mechanical properties of high-entropy alloys based on CoCrFeNi system, J. Alloy. Compd. 591 (2014) 11–21, https://doi.org/10.1016/j.jallcom.2013.12.210.
[6] K. Kishore, L.K. Meena, A.K. Chandan, M. Kawasaki, J. Gubicza, Corrosion behavior of coarse-grained and nanocrystalline Co33Ni33Cr19Mn15 and Co33Ni33Cr19Mn10Si5 multi-principal element alloys, Mater. Lett. 403 (2026) 139509, https://doi.org/10.1016/j.matlet.2025.139509.
[7] B. Schuh, B. Völker, V. Maier-Kiener, J. Todt, J. Li, A. Hohenwarter, Phase decomposition of a single-phase AlTiVNb high-entropy alloy after severe plastic deformation and annealing, Adv. Eng. Mater. 19 (2017), https://doi.org/10.1002/adem.201600674.
[8] Y. Kang, O. Cretu, J. Kikkawa, K. Kimoto, H. Nara, A.S. Nugraha, H. Kawamoto, M. Eguchi, T. Liao, Z. Sun, T. Asahi, Y. Yamauchi, Mesoporous multimetallic nanospheres with exposed highly entropic alloy sites, Nat. Commun. 14 (2023) 4182, https://doi.org/10.1038/s41467-023-39157-2.
[9] M. Krnel, A. Jelen, S. Vrtnik, J. Luzar, D. Gačnik, P. Koželj, M. Wencka, A. Meden, Q. Hu, S. Guo, J. Dolinšek, The effect of scandium on the structure, microstructure and superconductivity of equimolar Sc-Hf-Nb-Ta-Ti-Zr refractory high-entropy alloys, Materials 15 (2022) 1122, https://doi.org/10.3390/ma15031122.
[10] A.D. Pogrebnjak, A.A. Bagdasaryan, I.V. Yakushchenko, V.M. Beresnev, The structure and properties of high-entropy alloys and nitride coatings based on them, Russ. Chem. Rev. 83 (2014) 1027–1061, https://doi.org/10.1070/RCR4407.
[11] A.D. Pogrebnjak, I.V. Yakushchenko, A.A. Bagdasaryan, O.V. Bondar, R. Krause-Rehberg, G. Abadias, P. Chartier, K. Oyoshi, Y. Takeda, V.M. Beresnev, O.V. Sobol, Microstructure, physical and chemical properties of nanostructured (Ti–Hf–Zr–V–Nb)N coatings under different deposition conditions, Mater. Chem. Phys. 147 (2014) 1079–1091, https://doi.org/10.1016/j.matchemphys.2014.06.062.
[12] S.N. Grigoriev, O.V. Sobol, V.M. Beresnev, I.V. Serdyuk, A.D. Pogrebnyak, D. A. Kolesnikov, U.S. Nemchenko, Tribological characteristics of (TiZrHfVNbTa)N coatings applied using the vacuum arc deposition method, J. Frict. Wear 35 (2014) 359–364, https://doi.org/10.3103/S1068366614050067.
[13] O.N. Senkov, J.M. Scott, S.V. Senkova, F. Meisenkothen, D.B. Miracle, C. F. Woodward, Microstructure and elevated temperature properties of a refractory TaNbHfZrTi alloy, J. Mater. Sci. 47 (2012) 4062–4074, https://doi.org/10.1007/s10853-012-6260-2.
[14] O.N. Senkov, A.L. Pilchak, S.L. Semiatin, Effect of cold deformation and annealing on the microstructure and tensile properties of a HfNbTaTiZr refractory high entropy alloy, Metall. Mater. Trans. A 49 (2018) 2876–2892, https://doi.org/10.1007/s11661-018-4646-8.
[15] H. Huang, Y. Sun, P. Cao, Y. Wu, X. Liu, S. Jiang, H. Wang, Z. Lu, On cooling rates dependence of microstructure and mechanical properties of refractory high-entropy alloys HfTaTiZr and HfNbTiZr, Scr. Mater. 211 (2022) 114506, https://doi.org/10.1016/j.scriptamat.2022.114506.
[16] N. Yurchenko, V. Mirontsov, E. Mishunina, N. Stepanov, Effect of chemical composition variations in refractory Hf-Nb-Ta-Ti-Zr-Mo-V-Si complex concentrated alloys on the structure, mechanical properties, and oxidation behaviour, Mater. Charact. 222 (2025) 114856, https://doi.org/10.1016/j.matchar.2025.114856.
[17] Z. Liang, Y. Wu, Y. Miao, W. Pan, Y. Zhang, Composition design and tensile properties of additive manufactured low density Hf-Nb-Ta-Ti-Zr high entropy alloys based on atomic simulations, Materials 16 (2023) 4039, https://doi.org/10.3390/ma16114039.
[18] X.G. Wang, M. Sun, J.X. Liu, X.Q. Liu, Y.B. Ke, W.B. Jiang, H. Wang, Q.F. Fang, X. P. Wang, Effects of vanadium content on the microstructure and tensile properties of NbTiV Zr high-entropy alloys, J. Alloy. Compd. 987 (2024) 174227, https://doi.org/10.1016/j.jallcom.2024.174227.
[19] H. Chen, A. Kauffmann, S. Laube, I.-C. Choi, R. Schwaiger, Y. Huang, K. Lichtenberg, F. Müller, B. Gorr, H.-J. Christ, M. Heilmaier, Contribution of lattice distortion to solid solution strengthening in a series of refractory high entropy alloys, Metall. Mater. Trans. A 49 (2018) 772–781, https://doi.org/10.1007/s11661-017-4386-1.
[20] T. Vlasák, J. Čížek, O. Melikhova, F. Lukáč, D. Preisler, M. Janeček, P. Harcuba, M. Zimina, O. Srba, Thermal stability of microstructure of high-entropy alloys based on refractory metals Hf, Nb, Ta, Ti, V, and Zr, Metals 12 (2022) 394, https://doi.org/10.3390/met12030394.
[21] C. Chen, Y. Ma, M. Wei, X. Gai, Y. Peng, Y. Mei, X. Liu, K. Zhang, J. Li, Influence of increased TaNbV on the microstructure, mechanical properties, and energy release characteristics of high-entropy alloy HfZrTi(TaNbV)x, Materials 18 (2025) 4713, https://doi.org/10.3390/ma18204713.
[22] P. Nagy, M. Wątroba, Z. Hegedűs, J. Michler, L. Pethö, J. Schwiedrzik, Z. Czigány, J. Gubicza, Mapping the microstructure and the mechanical performance of a combinatorial Co–Cr–Cu–Fe–Ni–Zn high-entropy alloy thin film processed by magnetron sputtering technique, J. Mater. Res. Technol. 31 (2024) 47–61, https://doi.org/10.1016/j.jmrt.2024.06.059.
[23] A. Wang, L. Pethö, Z. Hegedűs, M. Wątroba, J. Michler, J. Veselý, P. Minárik, P. Nagy, J. Gubicza, High-entropy alloy mapping in the Co-Cr-Fe-Mo-Ni-W compositional library using a combinatorial thin film, J. Alloy. Compd. 1048 (2025) 185264, https://doi.org/10.1016/j.jallcom.2025.185264.
[24] J. Gubicza, Combinatorial design of novel multiprincipal element alloys using experimental techniques, Adv. Eng. Mater. 26 (2024), https://doi.org/10.1002/adem.202301673.
[25] W.C. Oliver, G.M. Pharr, An improved technique for determining hardness and elastic modulus using load and displacement sensing indentation experiments, J. Mater. Res. 7 (1992) 1564–1583, https://doi.org/10.1557/JMR.1992.1564.
[26] Y. Wu, J. Liu, Y. Zhang, Z. Li, E. Zhao, First-principles calculation for mechanical properties of TiZrHfNbTa series refractory high-entropy alloys, Mater. Today Commun. 40 (2024) 110165, https://doi.org/10.1016/j.mtcomm.2024.110165.
[27] F. Ren, Y. Hu, R. Qu, F. Liu, A composition design strategy for refractory high-entropy alloys, Materials 18 (2025) 4493, https://doi.org/10.3390/ma18194493.
[28] Y.X. Ye, B.L. Musico, Z.Z. Lu, L.B. Xu, Z.F. Lei, V. Keppens, H.X. Xu, T.G. Nieh, Evaluating elastic properties of a body-centered cubic NbHfZrTi high-entropy alloy – a direct comparison between experiments and ab initio calculations, Intermetallics 109 (2019) 167–173, https://doi.org/10.1016/j.intermet.2019.04.003.

[29] O.N. Senkov, D.B. Miracle, K.J. Chaput, J.-P. Couzinie, Development and exploration of refractory high entropy alloys—a review, J. Mater. Res. 33 (2018) 3092–3128, https://doi.org/10.1557/jmr.2018.153.
[30] G. Dirras, L. Lilensten, P. Djemia, M. Laurent-Brocq, D. Tingaud, J.-P. Couzinié, L. Perrière, T. Chauveau, I. Guillot, Elastic and plastic properties of as-cast equimolar TiHfZrTaNb high-entropy alloy, Mater. Sci. Eng. A 654 (2016) 30–38, https://doi.org/10.1016/j.msea.2015.12.017.
[31] E. Zalama, J. Gómez-García-Bermejo, R. Medina, J. Llamas, Road crack detection using visual features extracted by gabor filters, Comput. -Aided Civil. Infrastruct. Eng. 29 (2014) 342–358, https://doi.org/10.1111/mice.12042.
[32] O.N. Senkov, J.D. Miller, D.B. Miracle, C. Woodward, Accelerated exploration of multi-principal element alloys with solid solution phases, Nat. Commun. 6 (2015) 6529, https://doi.org/10.1038/ncomms7529.
[33] A.E. Nassar, A.M. Mullis, Rapid screening of high-entropy alloys using neural networks and constituent elements, Comput. Mater. Sci. 199 (2021) 110755, https://doi.org/10.1016/j.commatsci.2021.110755.
[34] R. Kozak, A. Sologubenko, W. Steurer, Single-phase high-entropy alloys – an overview, Z. Krist. Cryst. Mater. 230 (2015) 55–68, https://doi.org/10.1515/zkri-2014-1739.
[35] Y. Zhang, Y.J. Zhou, J.P. Lin, G.L. Chen, P.K. Liaw, Solid-solution phase formation rules for multi-component alloys, Adv. Eng. Mater. 10 (2008) 534–538, https://doi.org/10.1002/adem.200700240.
[36] X. Yang, Y. Zhang, Prediction of high-entropy stabilized solid-solution in multi-component alloys, Mater. Chem. Phys. 132 (2012) 233–238, https://doi.org/10.1016/j.matchemphys.2011.11.021.
[37] G. Carter, Preferred orientation in thin film growth — the survival of the fastest model, Vacuum 56 (2000) 87–93, https://doi.org/10.1016/S0042-207X(99)00171-2.
[38] D.J. Srolovitz, A. Mazor, B.G. Bukiet, Analytical and numerical modeling of columnar evolution in thin films, J. Vac. Sci. Technol. A Vac. Surf. Films 6 (1988) 2371–2380, https://doi.org/10.1116/1.575558.
[39] E. Kusano, Structure-zone modeling of sputter-deposited thin films: a brief review, Appl. Sci. Converg. Technol. 28 (2019) 179–185, https://doi.org/10.5757/ASCT.2019.28.6.179.
[40] S. Taheriniya, F.A. Davani, S. Hilke, M. Hepp, C. Gadelmeier, M.R. Chellali, T. Boll, H. Rösner, M. Peterlechner, C. Gammer, S.V. Divinski, B. Butz, U. Glatzel, H. Hahn, G. Wilde, High entropy alloy nanocomposites produced by high pressure torsion, Acta Mater. 208 (2021) 116714, https://doi.org/10.1016/j.actamat.2021.116714.
[41] S. Yang, J. Lu, F. Xing, L. Zhang, Y. Zhong, Revisit the VEC rule in high entropy alloys (HEAs) with high-throughput CALPHAD approach and its applications for material design-A case study with Al–Co–Cr–Fe–Ni system, Acta Mater. 192 (2020) 11–19, https://doi.org/10.1016/j.actamat.2020.03.039.
[42] S. Yang, G. Liu, Y. Zhong, Revisit the VEC criterion in high entropy alloys (HEAs) with high-throughput ab initio calculations: a case study with Al-Co-Cr-Fe-Ni system, J. Alloy. Compd. 916 (2022) 165477, https://doi.org/10.1016/j.jallcom.2022.165477.
[43] J.M. Sanchez, D. de Fontaine, The omega phase transformation, Le. J. De. Phys. Colloq. 38 (C7) (1977) 444–C7-452, https://doi.org/10.1051/jphyscol:1977788.
[44] P. Panjan, A. Drnovšek, N. Mahne, M. Čekada, M. Panjan, Surface topography of PVD hard coatings, Coatings 11 (2021) 1387, https://doi.org/10.3390/coatings11111387.
[45] E. Kusano, Revisitation of the structure zone model based on the investigation of the structure and properties of Ti, Zr, and Hf thin films deposited at 70–600 °C using DC magnetron sputtering, J. Vac. Sci. Technol. A 36 (2018) 041506, https://doi.org/10.1116/1.5036555.
[46] P. Nagy, M. Wątroba, Z. Hegedűs, J. Michler, L. Pethö, J. Schwiedrzik, Z. Czigány, J. Gubicza, Mapping the microstructure and the mechanical performance of a combinatorial Co–Cr–Cu–Fe–Ni–Zn high-entropy alloy thin film processed by magnetron sputtering technique, J. Mater. Res. Technol. 31 (2024) 47–61, https://doi.org/10.1016/j.jmrt.2024.06.059.
[47] P. Nagy, B. Kaszás, I. Csabai, Z. Hegedűs, J. Michler, L. Pethö, J. Gubicza, Machine learning-based characterization of the nanostructure in a combinatorial Co-Cr-Fe-Ni compositionally complex alloy film, Nanomaterials 12 (2022) 4407, https://doi.org/10.3390/nano12244407.
[48] P. Nagy, N. Rohbeck, R.N. Widmer, Z. Hegedűs, J. Michler, L. Pethö, J.L. Lábár, J. Gubicza, Combinatorial study of phase composition, microstructure and mechanical behavior of Co-Cr-Fe-Ni nanocrystalline film processed by multiple-beam-sputtering physical vapor deposition, Materials 15 (2022) 2319, https://doi.org/10.3390/ma15062319.
[49] J. Gubicza, X-Ray Line Profile Analysis in Materials Science, IGI Global, USA, 2014.
[50] S. Fritze, C.M. Koller, L. von Fieandt, P. Malinovskis, K. Johansson, E. Lewin, P. H. Mayrhofer, U. Jansson, Influence of deposition temperature on the phase evolution of HfNbTiVZr high-entropy thin films, Materials 12 (2019) 587, https://doi.org/10.3390/ma12040587.
[51] V. Vitek †, Core structure of screw dislocations in body-centred cubic metals: relation to symmetry and interatomic bonding, Philos. Mag. 84 (2004) 415–428, https://doi.org/10.1080/14786430310001611644.
[52] E. Clouet, B. Bienvenu, L. Dezerald, D. Rodney, Screw dislocations in BCC transition metals: from ab initio modeling to yield criterion, C. R. Phys. 22 (2021) 83–116, https://doi.org/10.5802/crphys.75.
[53] L. Dezerald, L. Proville, L. Ventelon, F. Willaime, D. Rodney, First-principles prediction of kink-pair activation enthalpy on screw dislocations in bcc transition metals: V, Nb, Ta, Mo, W, and Fe, Phys. Rev. B 91 (2015) 094105, https://doi.org/10.1103/PhysRevB.91.094105.
[54] A. Inoue, Bulk amorphous and nanocrystalline alloys with high functional properties, Mater. Sci. Eng. A 304-306 (2001) 1–10, https://doi.org/10.1016/S0921-5093(00)01551-3.
[55] A.S. Argon, Plastic deformation in metallic glasses, Acta Metall. 27 (1979) 47–58, https://doi.org/10.1016/0001-6160(79)90055-5.
[56] F. Spaepen, A microscopic mechanism for steady state inhomogeneous flow in metallic glasses, Acta Metall. 25 (1977) 407–415, https://doi.org/10.1016/0001-6160(77)90232-2.
[57] D. Pan, A. Inoue, T. Sakurai, M.W. Chen, Experimental characterization of shear transformation zones for plastic flow of bulk metallic glasses, Proc. Natl. Acad. Sci. 105 (2008) 14769–14772, https://doi.org/10.1073/pnas.0806051105.
[58] W.H. Wang, Elastic moduli and behaviors of metallic glasses, J. Non Cryst. Solids 351 (2005) 1481–1485, https://doi.org/10.1016/j.jnoncrysol.2005.03.024.
[59] J. Gu, M. Song, S. Ni, S. Guo, Y. He, Effects of annealing on the hardness and elastic modulus of a Cu36Zr48Al8Ag8 bulk metallic glass, Mater. Des. 47 (2013) 706–710, https://doi.org/10.1016/j.matdes.2012.12.071.
[60] W. Zhao, J.L. Cheng, S.D. Feng, G. Li, R.P. Liu, Intrinsic correlation between elastic modulus and atomic bond stiffness in metallic glasses, Mater. Lett. 175 (2016) 227–230, https://doi.org/10.1016/j.matlet.2016.03.037.
[61] O.P. Rachek, X-ray diffraction study of amorphous alloys Al–Ni–Ce–Sc with using Ehrenfest's formula, J. Non Cryst. Solids 352 (2006) 3781–3786, https://doi.org/10.1016/j.jnoncrysol.2006.05.031.
[62] P. Gupta, A. Gupta, A. Shukla, T. Ganguli, A.K. Sinha, G. Principi, A. Maddalena, Structural evolution and the kinetics of Cu clustering in the amorphous phase of Fe-Cu-Nb-Si-B alloy, J. Appl. Phys. 110 (2011), https://doi.org/10.1063/1.3622325.
[63] Y. Wu, F. Wang, Y. Huang, F. Zheng, Y. Zeng, Z. Lu, S. Wang, B. Sun, Y. Sun, A tantalum-containing zirconium-based metallic glass with superior endosseous implant relevant properties, Bioact. Mater. 39 (2024) 25–40, https://doi.org/10.1016/j.bioactmat.2024.04.014.
[64] S. Alvi, M. Milczarek, D.M. Jarzabek, D. Hedman, M.G. Kohan, N. Levintant-Zayonts, A. Vomiero, F. Akhtar, Enhanced mechanical, thermal and electrical properties of high-entropy HfMoNbTaTiVWZr thin film metallic glass and its nitrides, Adv. Eng. Mater. 24 (2022), https://doi.org/10.1002/adem.202101626.
[65] B. Jiang, J. Wang, L. Xu, C. Qian, T. Liu, J. Dai, X. Hou, Tunable mechanical properties of Ti-Zr-Ni-Cr-V amorphous ribbons via different melt spinning speeds during rapid solidification process, Materials 11 (2018) 947, https://doi.org/10.3390/ma11060947.
[66] B. Song, Y. Li, K. Wang, Z. Cong, B. Gao, Z. Song, J. Chen, Nano-mechanical properties of TaNbHfZr metallic glass films, Surf. Eng. 35 (2019) 728–735, https://doi.org/10.1080/02670844.2018.1558732.
[67] H.S. Chou, J.C. Huang, L.W. Chang, Mechanical properties of ZrCuTi thin film metallic glass with high content of immiscible tantalum, Surf. Coat. Technol. 205 (2010) 587–590, https://doi.org/10.1016/j.surfcoat.2010.07.042.
[68] S. Alvi, M. Milczarek, D.M. Jarzabek, D. Hedman, M.G. Kohan, N. Levintant-Zayonts, A. Vomiero, F. Akhtar, Enhanced mechanical, thermal and electrical properties of high-entropy HfMoNbTaTiVWZr thin film metallic glass and its nitrides, Adv. Eng. Mater. 24 (2022), https://doi.org/10.1002/adem.202101626.